A STUDY OF THE BASIC MECHANISMS OF DUST EROSION

CHARLES D. WOOD

SEPTEMBER 1963

Contract No. DA 23-072-ORD-1375
Task Order No. 17

DA Project Number Within
Army Materiel Command
1A025001A622 Formerly
DA Project Number
1A650212D622 and 5B98-09-004

SOUTHWEST RESEARCH INSTITUTE
SAN ANTONIO, TEXAS

DISTRIBUTION LIST

Distribution	Number of Copies
Director of Defense Research and Engineering Washington 25, D. C. Attn: Director Advanced Research Projects Agency	1
Director of Defense Research and Engineering Washington 25, D. C. Attn: Director or Ordnance Tactical Warfare Program	1
Chief of Research and Development Department of the Army Washington 25, D. C. Attn: Director of Army Research	2
Chief of Research and Development Department of the Army Washington 25, D. C. Attn: Director of Developments	1
Executive Secretary Army Scientific Advisory Panel c/o OCRD Washington 25, D. C.	1
Commander U. S. Army Research Office Box CM, Duke Station Durham, North Carolina Attn: CRD-AA-E	1
Commander U. S. Army Research Office Box CM, Duke Station Durham, North Carolina Attn: CRD-AA-I	1

DISTRIBUTION LIST (Cont'd)

Distribution	Number of Copies
Commander U. S. Army Research Office Box CM, Duke Station Durham, North Carolina Attn: CRD-AA-SS	1
Commander U. S. Army Research and Development Office, Panama P. O. Drawer 942 Fort Clayton, Canal Zone	1
Commanding General U. S. Army Combat Developments Command Fort Belvoir, Virginia Attn: CDCCD CDCMR CDCLN-AT CDCLN-MC	 1 1 1 1
Commander U. S. Army Combat Developments Center Fort Ord, California Attn: Ordnance Liaision Officer (USAOCDA), Bldg. 2870	1
Chief of Combat Developments Headquarters U. S. Army, Alaska APO 949 Seattle, Washington	1
Commanding General U. S. Army Materiel Command Building T-7 Washington 25, D. C. Attn: AMCRD-DW AMCRD-DM AMCRD-DS AMCRD-I AMCRD-RP AMCRD-SE	 1 1 1 1 1 1

DISTRIBUTION LIST (Cont'd)

Distribution	Number of Copies
Commanding General U. S. Army Materiel Command Washington 25, D. C. Attn: Mr. P. W. Espenschade, Project Officer AMCRD-RE	5
Commanding General U. S. Army Missile Command Redstone Arsenal, Alabama Attn: AMSMI-R	1
Commanding General U. S. Army Electronics Command Fort Monmouth, New Jersey Attn: AMSEL-RD	1
Commanding General U. S. Army Missile Command Redstone Arsenal, Alabama Attn: AMSMI-RC AMSMI-RHP AMSMI-RT	1 1 1
Commanding General U. S. Army Mobility Command Warren, Michigan 48090 Attn: AMSMO-RR AMSMO-RD	1 1
Commander Picatinny Arsenal MUCOM Dover, New Jersey Attn: SMUFA-DX	2
Commander Frankford Arsenal MUCOM Philadelphia, Pennsylvania 19137 Attn: SMUFA-1730	2

DISTRIBUTION LIST (Cont'd)

Distribution	Number of Copies
Commanding General U. S. Army Tank Automotive Center Warren, Michigan 48090	
Attn: SMOTA-RCE	1
SMOTA-RCL	1
SMOTA-RCP	1
SMOTA-REV	1
Commanding General U. S. Army Test and Evaluation Command Aberdeen Proving Grounds, Maryland	
Attn: AMSTE-TA	1
AMSTE-SA	1
STEAP-DS-DF	1
STEAP-DS-LU	1
D&PS Technical Library	1
Commanding General U. S. Army Weapons Command Rock Island, Illinois	
Attn: AMSWE-RDA	1
AMSWE-RDR	1
Director U. S. Army Coating and Chemical Laboratory Aberdeen Proving Ground, Maryland	1
Director U. S. Army Cold Regions Research and Engineering Laboratories P. O. Box 282 Hanover, New Hampshire	
Attn: Chief, Environmental Research Branch	1
Commander U. S. Army Foreign Science & Technology Center Room 4508, Munitions Building Washington 25, D. C.	
Attn AMXST-CM	1

DISTRIBUTION LIST (Cont'd)

Distribution	Number of Copies
Commander U. S. Army Harry Diamond Laboratories Van Ness & Connecticut Avenue, N. W. Washington 25, D. C.	
Attn: AMXDO-TIB	2
AMXDO-TSE	1
Director U. S. Army Human Engineering Laboratories Aberdeen Proving Ground, Maryland	
Attn. AMXHE-SUP	2
Commander U. S. Army Materials Research Agency Watertown, Massachusetts	1
Director U. S. Army Natick Laboratory Natick, Massachusetts	
Attn: Dr. W. K. Boyd	1
Director U. S. Army Natick Laboratory Natick, Massachusetts	
Attn: AMXRE-EE	1
Commander U. S. Army Engineer Research and Development Laboratories Fort Belvoir, Virginia	
Attn: SMOFB-KC	1
SMOFB-HS	1
Technical Document Center	1
President U. S. Army Arctic Test Board APO 733 Seattle, Washington	2

DISTRIBUTION LIST (Cont'd)

Distribution	Number of Copies
President U. S. Army Transportation Board Fort Eustis, Virginia	2
Commander Yuma Test Station Yuma, Arizona Attn: Test and Evaluation Division	2
Commander U. S. Army Engineer Waterways Experiment Station Vicksburg, Mississippi Attn: Mr. A. A. Maxwell	2
Commander U. S. Army Procurement District Office, St. Louis 4300 Goodfellow Blvd. St. Louis 20, Missouri Attn: AMXSL-KA	1
Chief U. S. Army Research and Development Group (9851) APO 757 New York, New York	1
Senior Standardization Representative U. S. Army Standardization Group, Canada Canadian Army Headquarters Ottawa 4, Ontario, Canada	1
U. S. Army Representative Headquarters Air Force Systems Command, USAF Andrews AFB Washington 25, D. C. Attn SCS-3	2

DISTRIBUTION LIST (Cont'd)

Distribution	Number of Copies
Chief of Naval Research Washington 25, D. C. Attn: Director Earth Sciences Division Assistant Chief for Research	1
Senior Marine & Amphibious Warfare Officer	1
Chief of Bureau of Yards and Docks Washington 25, D. C. Attn: Director Management Division Assistant Chief for RDT&E	5
Commander U. S. Naval Civil Engineering Research and Evaluation Laboratories Port Hueneme, California Attn: Chief, Environmental Division	1
Chief, Mechanical Engineering Department	1
Director Air Force Cambridge Research Laboratories Hanscon Field Bedford, Massachusetts Attn: Technical Reference Librarian	1
Chief Air Force Systems Command Scientific & Technical Liaison Office Main Navy Building 18th and Constitution Ave., N. W. Washington 25, D. C.	1
Commander Air Force Systems Command United States Air Force Wright-Patterson AFB, Ohio Attn: Chief, Environmental Division Engineering Test Directorate	2

DISTRIBUTION LIST (Cont'd)

Distribution	Number of Copies
Commander Air Proving Ground Center Air Force Systems Command United States Air Force Eglin AFB, Florida	2
Chief Air University Library Maxwell AFB, Alabama Attn: Document Acquisition Branch	1
Commander Defense Documentation Center 5010 Duke Street Cameron Station Alexandria, Virginia 22314	10
Scientific Information Officer Defense Research Staff British Embassy 3100 Massachusetts Avenue, N.W. Washington 8, D. C.	3
The Library of Congress Washington 25, D. C. Attn: Head, Bibliographical Section Reference Department Science and Technology Division	1
Director Office of Technical Services U. S. Department of Commerce Washington 25, D. C.	2
Director Prevention of Deterioration Center National Academy of Sciences National Research Council 2101 Constitution Avenue, N. W. Washington 25, D. C.	2

DISTRIBUTION LIST (Cont'd)

Distribution	Number of Copies
Mr. William H. Allen Special Publications Branch Office of Scientific & Technical Information, NASA 1875 Connecticut Avenue, N. W. Washington 25, D. C.	1
Head Research and Development Centralizing Activity for Shock, Vibration and Associated Environments Code 4021 U. S. Naval Research Laboratory Washington 25, D. C.	1
Director Washington Office Arctic Inst. of North America 1530 "P" Street, N. W. Washington 5, D. C.	1
Canadian Army Staff 2450 Massachusetts Avenue Washington 8, D. C. Attn: G50-1 A&R Section	3
Mr. Walter H. Ziegler Project Engineer Curtis-Wright Corporation Wright Aeronautical Division Wood Ridge, New Jersey	1
Professor Wolf E. Meyer 207 Mechanical Engineering Department Pennsylvania State University University Park, Pennsylvania	1
Dr. Louis Peltier Research Analysis Corporation 6935 Arlington Road Bethesda 14, Maryland	1

DISTRIBUTION LIST (Cont'd)

Distribution	Number of Copies
Chairman, SAE AGE-1C Military Support Equipment Committee (Mr. C. B. Rogers) c/o Clark Equipment Company Battle Creek, Michigan	1
Chairman, SAE CIMTC Subc. XV (Environment) (Mr. Paul Gilson) c/o SMOEP-6, U. S. Army Engineer Procurement Office, Chicago 226 W. Jackson Boulevard Chicago 6, Illinois	2
Mr. W. P. Gardner Director of Environmental Testing Sandia Corporation Sandia Base Albuquerque, New Mexico	2
Mr. James S. Arnold Physics Department Building 108 Stanford Research Institute 330 Ravenswood Avenue Menlo Park, California	1
Dr. Robert Rowe Dean of Engineering Vanderbilt University Nashville 5, Tennessee	1

A STUDY OF THE BASIC MECHANISM OF DUST EROSION

Charles D. Wood

June 1963

Contract No.
DA-23-072-ORD-1375
Task Order No. 17

DA Project No. within
Army Materiel Command
1A025001A622
Formerly DA Project No.
1A650212D622 and
5B98-09-004

SwRI Report No. AR-499

Southwest Research Institute
Department of Automotive Research
8500 Culebra Road
San Antonio, Texas 78206

ABSTRACT

This report presents the results of a study of the erosion of materials by air-borne dust. Erosion rates for several metals were obtained over a wide range of dust particle velocity, particle angle of impact, dust particle size, and dust concentration.

The experimental results show that for the range of variables studied, erosion occurs due to the plastic displacement of material by the dust particle. Relationships defining the effect of particle velocity and angle of impact upon erosion rates are given. Experimental data showing the effects of dust concentration, dust size distribution, and material properties on the rates of erosion are presented, and the mechanisms discussed.

TABLE OF CONTENTS

		Page
LIST OF ILLUSTRATIONS		iv
LIST OF TABLES		vi
LIST OF SYMBOLS		vii
I.	INTRODUCTION	1
II.	PROCEDURE	2
A.	Equipment	2
B.	Experimental Procedure	2
C.	Test Specimens	5
D.	Dust	5
E.	Accuracies of Controlled Parameters	7
III.	RESULTS	12
A.	Theoretical Analysis	12
B.	Angle of Impact Effect	15
C.	Erosion Wear Patterns	22
D.	Velocity Effect	25
E.	Concentration Effect	31
F.	Dust Size Effect	33
G.	Material Properties Effect	36
IV.	CONCLUSIONS AND RECOMMENDATIONS	42
LIST OF REFERENCES		44
APPENDIXES		
A.	Derivation of Particle Distance - Velocity Relationship	45
B.	Estimation of True Impact Angle	47

LIST OF ILLUSTRATIONS

Figure		Page
1	Experimental Setup	3
2	Dust Particle Size Distribution	8
3	Calculated Particle Velocity	10
4	Removal of Material by an Abrasive Particle	12
5	Predicted Volume Removal by a Single Abrasive Particle	14
6	Nozzle Specimen Geometry	15
7	Weight Loss Factor Versus Test Impact Angle, Martensitic C-1050 Steel, Air Velocity 475 fps, Dust Concentration 0.011 gr/ft^3, 0 - 74 Micron Silica Flour	16
8	Weight Loss Factor Versus Test Impact Angle, Pearlitic C-1050 Steel, Air Velocity 475 fps, Dust Concentration 0.011 gr/ft^3, 0 - 74 Micron Silica Flour	16
9	Weight Loss Factor Versus Test Impact Angle, Tempered C-1050 Steel, Air Velocity 475 fps, Dust Concentration 0.011 gr/ft^3, 0 - 74 Micron Silica Flour	17
10	Weight Loss Factor Versus Test Impact Angle, Martensitic C-1050 Steel, Air Velocity 835 fps, Dust Concentration 0.013 gr/ft^3, 0 - 74 Micron Silica Flour	17
11	Weight Loss Factor Versus Test Impact Angle, Pearlitic C-1050 Steel, Air Velocity 835 fps, Dust Concentration 0.013 gr/ft^3, 0 - 74 Micron Silica Flour	18

LIST OF ILLUSTRATIONS (Cont'd)

Figure		Page
12	Weight Loss Factor Versus Test Impact Angle, Tempered C-1050 Steel, Air Velocity 835 fps, Dust Concentration 0.013 gr/ft^3, 0 - 74 Micron Silica Flour	18
13	Weight Loss Factor Versus Test Impact Angle, 6061-T6 Aluminum Alloy, Air Velocity 835 fps, Dust Concentration 0.013 gr/ft^3, 0 - 74 Micron Silica Flour	19
14	Weight Loss Factor Versus Test Impact Angle, Pearlitic C-1050 Steel, Air Velocity 835 fps, Dust Concentration 0.013 gr/ft^3, SAE Test Dust, Coarse Grade	19
15	Weight Loss Factor Versus Test Impact Angle, Pearlitic C-1050 Steel, Air Velocity 835 fps, Dust Concentration 0.013 gr/ft^3, SAE Test Dust, Fine Grade	20
16	Erosion Ripple Pattern-Lead Specimen	23
17	Weight Loss Factor Versus Air Velocity, Martensitic C-1050 Steel, Dust Concentration 0.013 gr/ft^3, 0 - 74 Micron Silica Flour	26
18	Weight Loss Factor Versus Air Velocity, Pearlitic C-1050 Steel, Dust Concentration 0.013 gr/ft^3, 0 - 74 Micron Silica Flour	27
19	Weight Loss Factor Versus Air Velocity, Tempered C-1050 Steel, Dust Concentration 0.013 gr/ft^3, 0 - 74 Micron Silica Flour	28
20	Weight Loss Factor Versus Air Velocity, 6061-T6 Aluminum Alloy, Dust Concentration 0.013 gr/ft^3, 0 - 74 Micron Silica Flour	29

LIST OF ILLUSTRATIONS (Cont'd)

Figure		Page
21	Weight Loss Factor Versus Dust Concentration, Air Velocity 475 fps, Test Impact Angle 90°, 0 - 74 Micron Silica Flour	32
22	Weight Loss Factor Versus Dust Concentration, Air Velocity 475 fps, Test Impact Angle 90°, 0 - 74 Micron Silica Flour	32
23	Weight Loss Factor Versus Dust Particle Size Range, Air Velocity 850 fps, Dust Concentration 0.013 gr/ft^3, Pearlitic C-1050 Steel, 40° Test Impact Angle, Silica Flour	35
24	Average Weight Loss Per Impact Versus Dust Particle Size Range, Air Velocity 850 fps, Dust Concentration 0.013 gr/ft^3, Pearlitic C-1050 Steel, 40° Test Impact Angle, Silica Flour	35
25	Volume Loss Factor Versus Knoop Hardness Number, Airstream Velocity 835 fps, 0 - 74 Micron Silica Flour, Dust Concentration 0.013 gr/ft^3, 90° Impact Angle	37
26	Volume Loss Factor Versus Knoop Hardness Number × % Elongation, Airstream Velocity 835 fps, 0 - 74 Micron Silica Flour, Dust Concentration 0.013 gr/ft^3, 90° Impact Angle	37
27	Specific Energy of Volume Removal Versus Depth of Cut for Grinding Tests	39

LIST OF TABLES

Table		Page
I	Specimen Material Properties	6

LIST OF SYMBOLS

Symbol		Unit
A	Specimen area	in^2
$\overline{A}$	Particle projected area	ft^2
a	Nozzle exit area	in^2
c	Dust concentration	gr dust/scf
C_R	Spherical particle drag coefficient	
d	Particle diameter	ft
$F(y_T)$	Projected contact area between abrasive particle and material	ft^2
I	Moment of inertia of abrasive particle	$lb_m\text{-}ft^2$
K	Ratio of vertical to horizontal force on abrasive particle	
m	Mass of single abrasive particle or mass of group of particles of equal diameter	lb_m
M	Mass of all particles in sample	lb_m
N	Number of particle impacts on specimen	$in^{-2}sec^{-1}$
N_{max}	Maximum number of particle impacts on specimen	$in^{-2}sec^{-1}$
p	Plastic flow stress of material	psi
Q	Total air flow through nozzle	scfm
q	Volume of material removed by a single abrasive particle	ft^3
R	Particle Reynold's number	

LIST OF SYMBOLS (Cont'd)

Symbol		Unit
R_o	Initial particle Reynold's number	
r	Distance from cutting tip to c.g. of abrasive grain	ft
t	Time	sec
u	Dust feeder calibration (weight of dust per inch of groove)	gr/in.
V	Particle speed	ft/sec
v	Dust feeder piston speed	in./min
W	Airstream velocity	ft/sec
w	Weight loss factor	$gr/in.^2 gr$
x	Distance of particle travel through nozzle	ft
x_G, y_G	Coordinates of center of gravity of abrasive particle	ft
x_T, y_T	Corrdinates of cutting tip of abrasive particle	ft
$\dot{x}'_T$	Horizontal particle tip velocity when cutting is complete	ft/sec
α	Actual particle-specimen impact angle	degrees
θ	Test impact angle	degrees
μ	Viscosity of air in airstream	$lb/ft^{-1}sec^{-1}$
ρ	Particle density	lb/ft^3
ρ_o	Density of air in airstream	lb/ft^3

Symbol		Unit
ϕ	Angle of rotation of abrasive particle about center of gravity	degrees
ψ	Ratio of projected area of particle-specimen contact to area of contact below orignal surface	

I. INTRODUCTION

Recent investigations[1]* at Southwest Research Institute have conclusively shown that gas turbine performance and endurance is severely limited by ingestion of small amounts of air-borne dust. The results of dust ingestion are erosion of shrouds, turbine and compressor blading, and diffusers to the extent that the machine may be destroyed in a few hours of operation. The trend towards use of gas turbine power-plants in military ground vehicles urgently requires a solution to this problem.

In order to effect a systematic approach to a solution to the problem of erosion by air-borne dust, it became evident that a basic understanding of the mechanisms of dust erosion was needed. To this end this investigation was directed. Specifically, this investigation deals with the influence of various parameters upon the rate of erosion of several metals. These parameters are dust particle velocity, particle angle of impact, particle size, particle concentration in the transporting air stream, and the properties of the material being eroded.

Although the primary objective of this study is to provide information for the improvement of gas turbines operating in a dusty atmosphere, the results can be applied to a better understanding of dust erosion in general, within the range of the various parameters used in this investigation. Each parameter was varied in a range as dictated by published data on the characteristics of natural air-borne dust[2], and on the operating parameters of typical gas turbine machines. The ranges of the various parameters in the experimental investigation were as follows:

Parameter	Range
Dust size distribution	0-5 micron to 0-150 micron
Dust particle velocity	150 to 900 fps
Dust concentration	0.00027 to 0.0275 gr dust/scf air
Dust particle angle of impact	20 to 90°

The eroded materials varied from lead (Knoop hardness 4.6) to martensitic steel (Knoop hardness 750).

*Numbered superscripts indicate correspondingly numbered references in List of References.

II. PROCEDURE

A. Equipment

The experimental setup is shown schematically in Figure 1. The air flow from a 220 scfm air compressor is directed through a shutoff valve, through a large air dryer containing a desiccant, through an orifice plate, and then to the air nozzle. Upstream of the air nozzle, the required weight rate of dust is introduced into the air stream.

This flow of dust originates from a dust feeder, consisting of a hydraulic cylinder, a grooved plate, and a dust pickup. Air pressure is maintained on the piston end of the cylinder, and the blind end of the cylinder is filled with water. Water is allowed to flow from the blind end port through a needle valve and a flowmeter, thence to a drain. The speed of piston travel may be regulated and measured by the needle valve and flowmeter respectively. Connected to the end of the piston is a flexible tube, which leads to the suction port of an air ejector. As the piston retracts, it draws the end of the flexible tube along a dust-filled groove in a plate located under the piston. The air flow developed by the air ejector in the flexible tube draws in the dust from the groove, and introduces it into the main air stream. The air ejector is powered by a high pressure flow of air. The pressure and flow rate of this air flow are measured and controlled by a flowmeter, pressure gage, and a shutoff valve.

The dust/air mixture leaving the nozzle impinges on the material specimen held in an adjustable specimen holder. The specimen holder can be rotated to vary the angle of impact of the dust particles on the specimen. The axis of rotation lies in the plane containing the specimen surface so that the nozzle exit-specimen distance does not vary with angle of attack. The air-dust mixture after leaving the nozzle is contained in a shroud, and exhausted to atmosphere outside the laboratory.

B. Experimental Procedure

Prior to all experiments, it was necessary to calibrate the dust feeding device. This was done by filling the grooves in the grooved plate with dry dust, and then weighing the dust held in the grooves. After many trials, a technique of filling the grooves was found that resulted in repeatable dust weights. By dividing the dust weight by the groove lengths, a value for dust weight per unit length of groove was obtained. This procedure was repeated for each dust size range and dust type used in the tests.

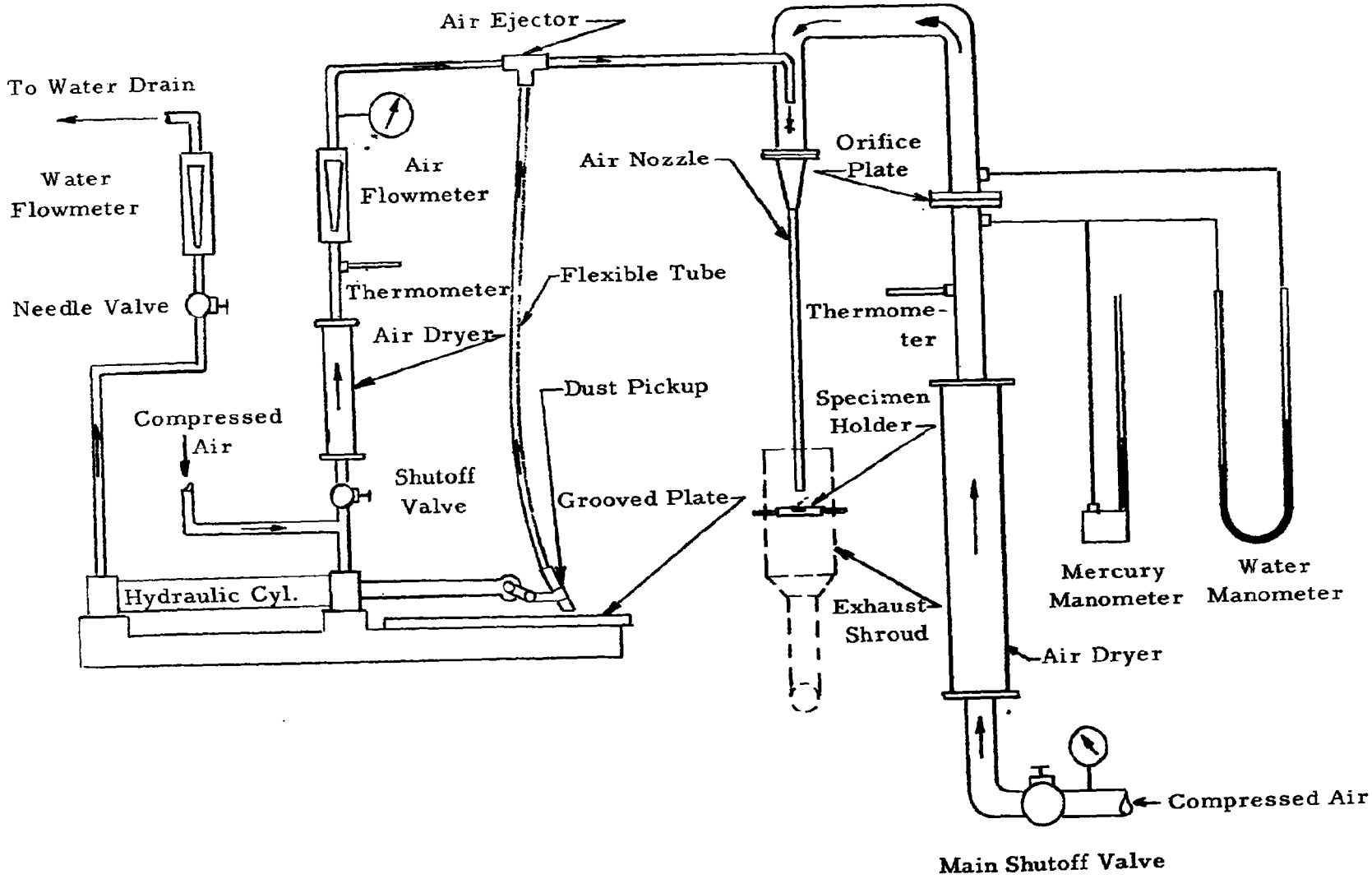

FIGURE 1. EXPERIMENTAL SETUP

The piston rate of travel was correlated with the water flowmeter reading experimentally. Then, by reading water flow rate (piston speed), the weight rate of dust injected into the main air stream could be calculated for any dust size or type.

A typical run was conducted as follows: A weighed specimen was installed in the specimen holder, and the holder oriented to the desired angle. The flow of high pressure air to the ejector was started, and adjusted to provide an adequate suction flow through the flexible tube. The main shutoff valve was opened and adjusted to provide the required air flow as indicated by the orifice plate manometers. Then the piston speed was adjusted by manipulation of the needle valve to obtain the desired dust feed rate. The test was terminated after a certain weight of dust had been used, usually 70 or 80 grams. The specimen was then reweighed to determine the weight loss. The dust concentration was calculated as

$$c = \frac{uv}{Q} \tag{1}$$

where the symbols are as defined in the List of Symbols. The total air flow Q is given as

$$Q = Q_1 + Q_2 \tag{2}$$

The main air flow Q_1 was calculated using the standard orifice equations. The dust injection air flow Q_2 was read directly from the air ejector flowmeter and corrected to standard conditions.

The average air velocity at the nozzle exit was calculated directly from the total flow Q, the measured nozzle area at the exit, and the experimentally verified fact that the air flow was essentially isothermal downstream from the main shutoff valve. The suction flow to the air ejector was neglected, since it was found to be small compared to the measured flows.

A survey of the air velocity at the nozzle exit was made with a pitot tube. This served to verify the calculated average air velocity, and showed that the air velocity was essentially constant over the extent of the specimen. From the pitot tube data, a factor was obtained to convert average air velocity experienced by the specimen; in other words, a correction for nozzle boundary layer effects was used.

Specimen weight losses due to erosion are presented as specimen weight loss per unit specimen area, per unit weight of dust impinging on the specimen. This factor is denoted by the term "weight loss factor." The "volume loss factor" is the weight loss factor divided by the specimen material density.

C. Test Specimens

Table I presents the properties of the materials tested.

Prior to each test, the specimen was polished to remove surface scratches, and then weighed on an analytical balance. The specimen was weighed twice before the test, and twice afterwards, the weight loss being computed from the average weights. Weights were recorded to the nearest tenth of a milligram, and the average weight seldom differed from the extreme by more than two tenths of a milligram.

The specimens were stored in a desiccator, and were handled by tweezers to prevent contamination of the surfaces. Before weighing, the specimens were carefully cleaned to remove air-borne particles.

Each specimen was approximately 3/8 in. square, and .060 in. thick. This relatively small size was dictated by considerations of nozzle area, air velocity, and available compressor capacity. The resulting small specimen weight contributes to more accurate weight loss measurements, since for heavy specimens the weight loss is the small difference between two large numbers, with the attending inaccuracies.

D. Dust

For the majority of the erosion experiments, the dust used was silica flour, with the following typical chemical analysis:

Component	% by Weight
Silicon dioxide (S_iO_2)	99.90
Iron Oxide (Fe_2O_3)	0.018
Aluminum Oxide (Al_2O_3)	0.12
Titanium dioxide (TiO_2)	0.007
Calcium Oxide (CaO)	0.01
Magnesium Oxide (MgO)	Trace

The silicon dioxide in this dust is present in the form of quartz, with a Moh's hardness of 7.

For comparison purposes, several tests were run using the two grades of SAE test dust[3] with the following chemical analysis:

TABLE I. SPECIMEN MATERIAL PROPERTIES

Material	Knoop Hardness, KG/mm^2	Density, gr/cc	Tensile Strength, psi $\times 10^{-3}$	Elongation in 2 Inches, %
C-1050 Steel (Martensitic)	750*	7.80	375	5
C-1050 Steel (Tempered)	336*	7.80	128	23
C-1050 Steel (Pearlitic)	192*	7.80	102	30
303 Stainless Steel	190*	7.93	100	50
Copper	63*	8.92	34	45
6061-T6 Aluminum	65*	2.65	45	12
6061-0 Aluminum	43*	2.65	18	25
Lead	4.6*	11.3	1.9	100

*Measured values - all other values estimated from handbook data.
(All Knoop hardness numbers determined using 200 gram load.)

Component	% by Weight
Silicon dioxide (SiO_2)	67 to 69
Iron Oxide (Fe_2O_3)	3 to 5
Aluminum Oxide (Al_2O_3)	15 to 17
Calcium Oxide (CaO)	2 to 4
Magnesium Oxide (MgO)	0.5 to 1.5
Total Alkalis	3 to 5
Ignition Loss	2 to 3

More significant in dust erosion studies is the mineral identity of the dust, as shown below for the SAE test dust:

Mineral Identity	% by Weight	Moh's Hardness
Plagioclase Feldspars	65 - 70	6 - 6.5
Quartz	15 - 18	7
Amphibole Hornblende	10 - 12	5 - 6
Vesuvianite	0.5 - 1	6.5
Muscovite Mica	Approx. 0.5	2.5 - 3
Biotite Mica	Approx. 0.5	2.5 - 3
Tourmaline	Approx. 0.5	7 - 7.5

The size distributions of the dusts used in this study are shown in Figure 2.

E. Accuracies of Controlled Parameters

To determine the effect of the various parameters upon the rate of erosion, the parameter being investigated was assigned a different value for each test in a series of tests while the other parameters were held at a constant value for the complete series. The dependent variable, weight loss, was measured for each test. Certain inherent characteristics of the experimental setup introduced a margin of error in the value of these controlled parameters.

The primary source of error in the controlled parameters arises from the dynamics of the dust particles in the air stream. The particles are introduced into the streamwith some initial velocity and are then accelerated by the airstream until they impinge upon the specimen. The impinging velocity of the particles depends upon their size, weight, shape, and upon the velocity, pressure, and temperature of the airstream. Other factors being constant, the smaller particle will more nearly attain the airstream velocity than the larger particle.

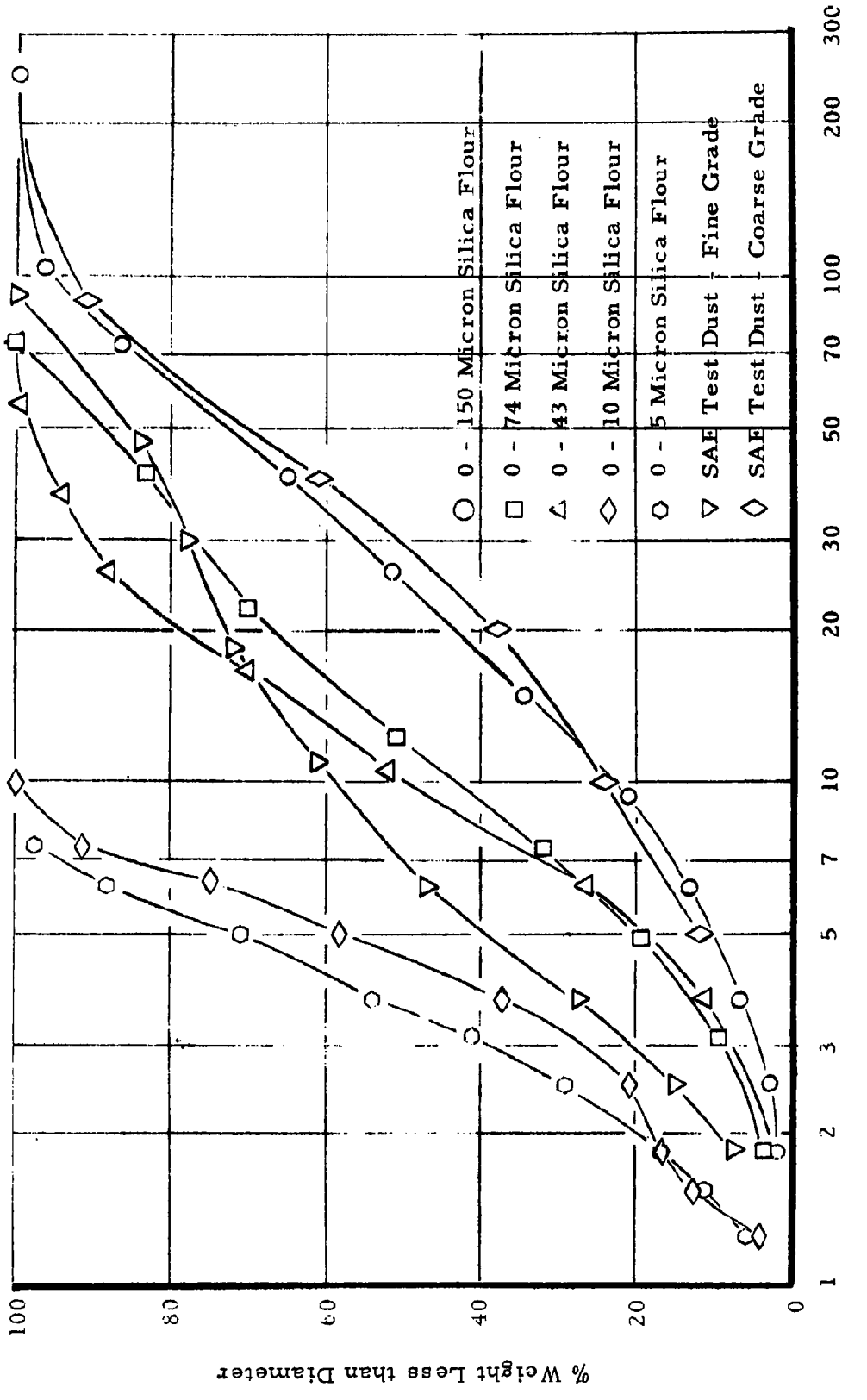

FIGURE 2. DUST PARTICLE SIZE DISTRIBUTION

In the neighborhood of the specimen, the airstream deflects around the specimen. Dust particles in this stream are thus subjected to drag forces acting to change the particle direction of travel. This causes the dust particles to strike the specimen at angles other than the test angle. Throughout this report, the test impact angle will be defined as the angle between the specimen and the nozzle centerline. The actual angle of impact is defined as the angle between the velocity vector of a particular particle and the specimen at the instant of contact. The difference between these two angles increases with decreasing particle size, decreasing air velocities, and increasing impact angles.

An estimation of the velocity error may be obtained from a solution of the particle one-dimensional equation of motion. From Dallavalle[4], the drag coefficient for spherical particles is

$$C_R = 0.4 + \frac{40}{R} \quad (2 < R < 500) \tag{3}$$

where

$$R = \frac{\rho_o d}{\mu} (W - V) \tag{4}$$

It may be shown (see Appendix A) that for dust particles less than approximately 150 microns in diameter in an airstream of normal temperature, the distance-velocity relationship of the dust particle is given by

$$\frac{\rho_o}{\rho} \frac{x}{d} = \frac{R_o}{30} \left[\log \frac{R + 100}{R_o + 100} \frac{R_o}{R} \right] + 3 \frac{1}{3} \log \left(\frac{R + 100}{R_o + 100} \right) \tag{5}$$

where

$$R_o = \frac{\rho_o d}{\mu} W \tag{6}$$

The drag coefficient for higher particle Reynold's numbers is given[4] by

$$C_R = 0.44 \quad (500 < R < 10^4) \tag{7}$$

Thus, it is seen that Equation (5) is more approximate but still useful at Reynold's numbers greater than the range indicated by Equation (3). Solutions to Equation (5) are shown graphically in Figure 3, for the nozzle

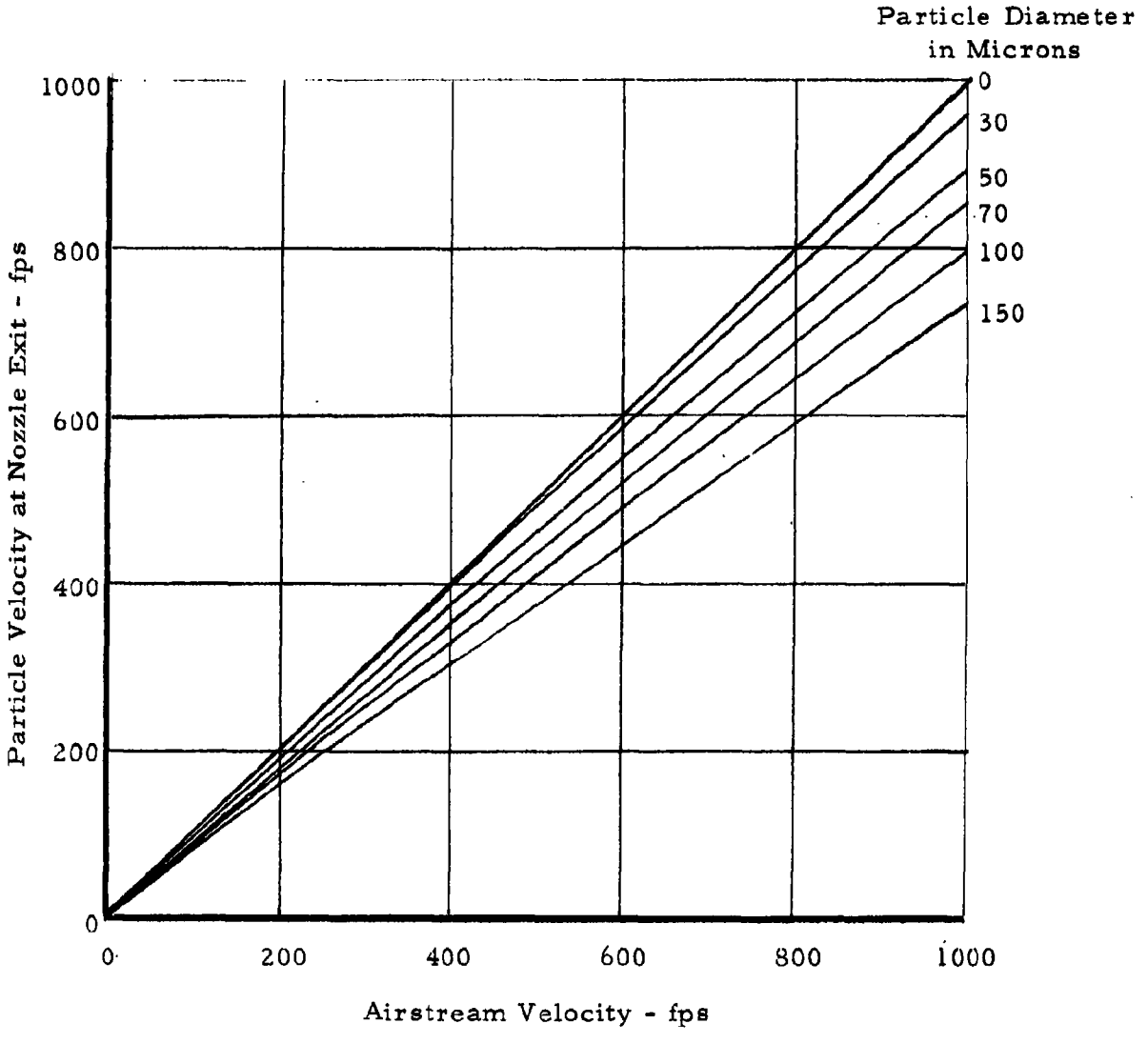

FIGURE 3. CALCULATED PARTICLE VELOCITY

length used in the experiments (5 feet) and for various particle sizes. The consequences of the deviation of particle velocity from the nozzle air velocity will be considered elsewhere in this report.

The determination of the true impact angle of the dust particle on the specimen presents considerable difficulties. An experimental technique was devised to make a rough approximation of the maximum error in impact angle. A glass specimen was placed in the specimen holder, oriented to obtain a test impact angle of 90°, and impinged with a small amount of 0-5 micron dust at approximately 500 feet per second air velocity. The glass specimen was then inspected under a microscope, and the number and location of the resulting pits in the glass recorded. For a first approximation, it can be shown that (see Appendix B)

$$\sin \alpha = \frac{N}{N_{max}} \sin \theta \tag{8}$$

Using Equation (8), α was calculated to be approximately 40°, the error in this case being roughly 60°.

For dust in the size range 50-74 microns, at the same air velocity and test angle, α was found to be essentially 90°; that is, the actual angle was approximately equal to the test angle.

The 60° error for the 0-5 micron dust is considered an extreme case, and the average error for the large majority of the tests is probably much lower than this value. The effects of this error can be seen, however, and will be considered again in the discussion of the test results.

III. RESULTS

A. Theoretical

In a paper by Finnie[5], a theoretical analysis of the volume of material removed by an impinging abrasive grain is presented. A summary of this analysis is presented below.

Figure 4 shows an idealized representation of an abrasive particle removing material from a surface. The objective of the analysis is to determine the equation of motion of the particle through the surface, thus allowing an estimation of the volume of material removed.

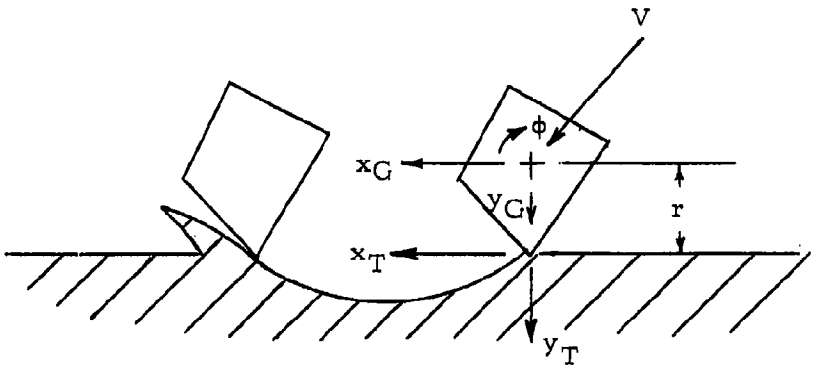

FIGURE 4. REMOVAL OF MATERIAL BY AN ABRASIVE PARTICLE

Several assumptions are required. First, it is assumed that the particle has no initial rotation. It is very probable that actually the particles have rotations in all directions, but it seems reasonable to take the assumption as an average condition.

Since it may be shown that the particle rotation during cutting is small, it is assumed that

$$y_T \approx y_G$$
$$x_T \approx x_G + r\phi \qquad (9)$$

It is further assumed that the force on the particle during cutting will be proportional to the area of contact times a plastic flow stress p. The ratio of the vertical to horizontal force on the particle (K) is assumed to be constant during cutting, in view of the first and second assumptions.

Then, the equations of motions may be written as

$$m\ddot{y}_T + pKF(y_T) = 0 \tag{10}$$

$$m\ddot{x}_T + p\left(1 + \frac{mr^2}{I}\right)F(y_T) = 0 \tag{11}$$

The term $F(y_T)$ is the projected area of particle-surface contact on the vertical plane. The initial conditions are given as

$$\dot{x}_T = V \cos \alpha \tag{12}$$

$$\dot{y}_T = V \sin \alpha \tag{13}$$

The incremental volume removed is

$$dq = \frac{F(y_T)}{\psi} dx_T \tag{14}$$

where ψ is the ratio of the projected area of contact to the projected area of contact underneath the original surface.

Integrating Equation (14) after substituting for $F(y_T)$ from Equation (11) yields

$$q = \frac{mV^2}{2p\left(1 + \frac{mr^2}{I}\right)}\left[\cos^2 \alpha - \left(\frac{\dot{x}_T'}{V}\right)^2\right] \tag{15}$$

where $\dot{x}_T'$ is the horizontal velocity of the particle tip when cutting is complete.

One end condition is $\dot{x}_T' = 0$, then

$$q = \frac{mV^2}{2p\left(1 + \frac{mr^2}{I}\right)} \cos^2 \alpha \tag{16}$$

If the particle tip still has horizontal velocity when cutting is complete, it can be shown that for this case

$$q = \frac{mV^2}{2p\left(1 + \frac{mr^2}{I}\right)} \quad \frac{2}{P}\left[\sin 2\alpha - \frac{2\sin^2 \alpha}{P}\right] \tag{17}$$

where

$$P = \frac{K}{1 + \frac{mr^2}{I}} \tag{18}$$

Equations (16) and (17) are equal for $\tan \alpha = P/2$. Maximum volume removal occurs for $\tan 2\alpha = P$. Equation (16) is valid for $\tan^{-1} P/2 < \alpha < 90°$ and Equation (17) is to be used for $0 < \alpha < \tan^{-1} P/2$. Equations (16) and (17) predict that for a single particle, the volume removed is proportional to the particle velocity squared, and inversely proportional to the flow stress of the material. In addition, it is predicted that the volume removed will exhibit a maximum when plotted versus impact angle α, the angle for maximum erosion dependent on the parameter P. Equation (17) shows that for an impact angle of zero degrees, the volume loss is zero. Also for an impact angle of 90°, Equation (16) predicts no volume loss. Figure 5 shows the theoretical results plotted for several values of the parameter P.

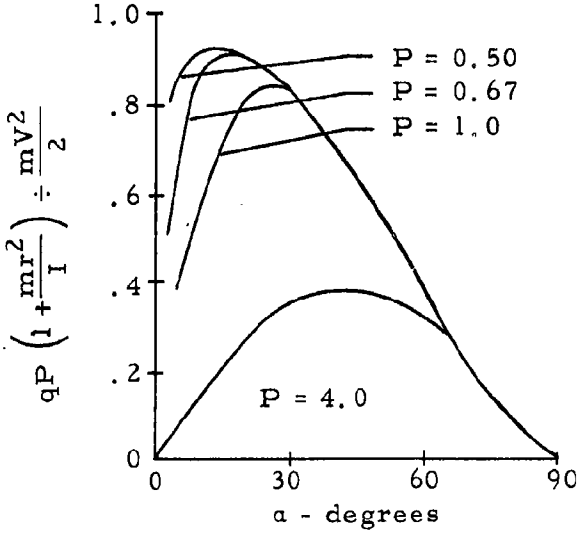

FIGURE 5. PREDICTED VOLUME REMOVAL FOR A SINGLE ABRASIVE PARTICLE

B. Angle of Impact Effect

The effect of angle of impact upon material erosion will be presented using the weight loss factor as a measure of the erosion rate. Before discussing the results obtained, the method of calculating this factor should be considered. As previously explained, the weight loss factor is the weight of material eroded per unit specimen area per unit weight of dust impinged on the specimen. From Figure 6 it is seen that the weight of dust impinging on the specimen varies with the angle of impact.

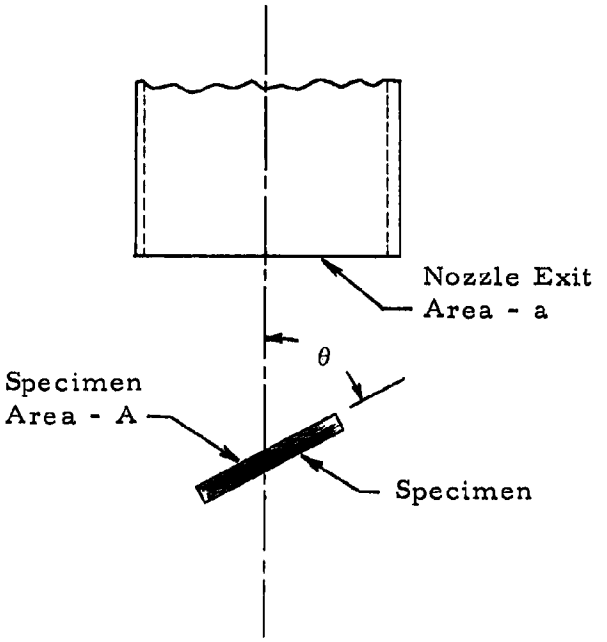

FIGURE 6. NOZZLE-SPECIMEN GEOMETRY

The weight of dust striking the specimen is given by (total weight of dust leaving nozzle) $\times \left(\frac{A \sin \theta}{a} \right)$. Then the weight loss factor is expressed as

$$\frac{\text{weight eroded}}{(A)\ (\text{wt of dust striking specimen})} = \frac{(\text{weight eroded})\ (a)}{(A^2)\ (\text{total dust wt})\ (\sin \theta)}$$

The effect of test angle of impact upon erosion rate is shown in Figures 7 through 15. In several of the graphs, there is considerable scatter of data, especially at low angles of impact. The manner in which to draw the curves to best fit these data is certainly not obvious. However

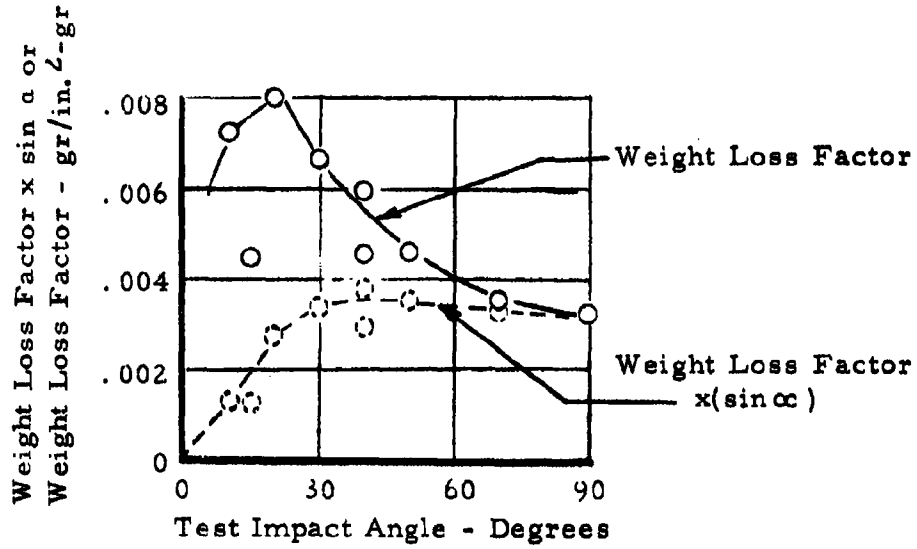

FIGURE 7. WEIGHT LOSS FACTOR VERSUS TEST IMPACT ANGLE, MARTENSITIC C-1050 STEEL, AIR VELOCITY 475 FPS, DUST CONCENTRATION 0.011 GR/FT^3, 0 - 74 MICRON SILICA FLOUR

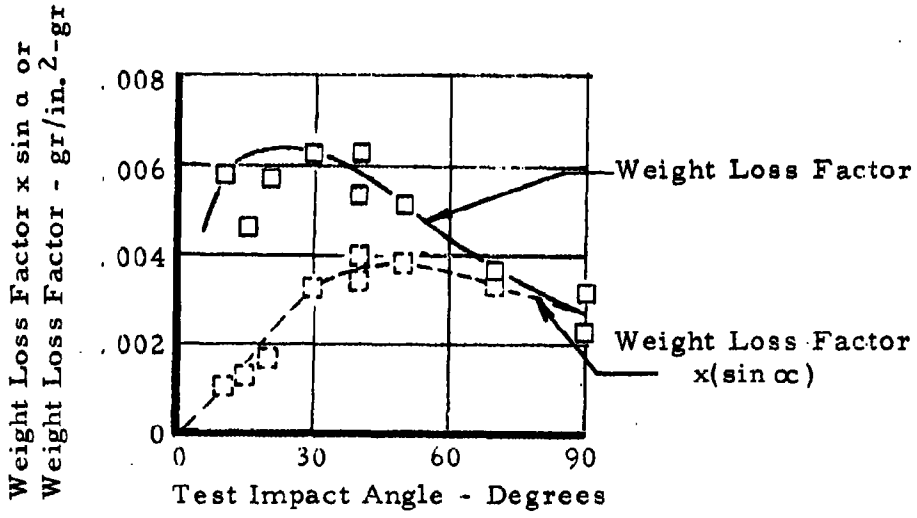

FIGURE 8. WEIGHT LOSS FACTOR VERSUS TEST IMPACT ANGLE, PEARLITIC C-1050 STEEL, AIR VELOCITY 475 FPS, DUST CONCENTRATION 0.011 GR/FT^3, 0 - 74 MICRON SILICA FLOUR

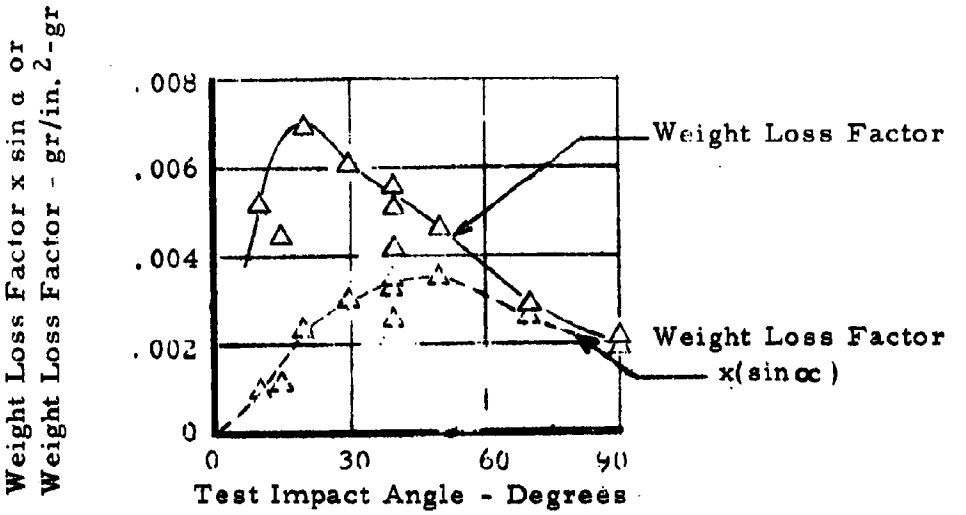

FIGURE 9. WEIGHT LOSS FACTOR VERSUS TEST IMPACT ANGLE, TEMPERED C-1050 STEEL, AIR VELOCITY 475 FPS, DUST CONCENTRATION 0.011 GR/FT^3, 0 - 74 MICRON SILICA FLOUR

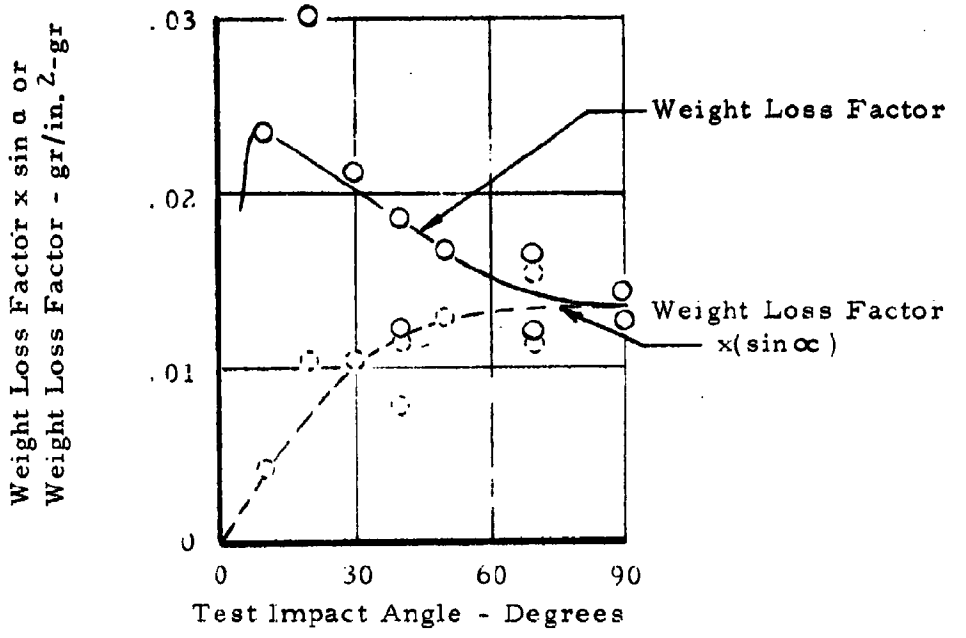

FIGURE 10. WEIGHT LOSS FACTOR VERSUS TEST IMPACT ANGLE, MARTENSITIC C-1050 STEEL, AIR VELOCITY 835 FPS, DUST CONCENTRATION 0.013 GR/FT^3, 0 - 74 MICRON SILICA FLOUR

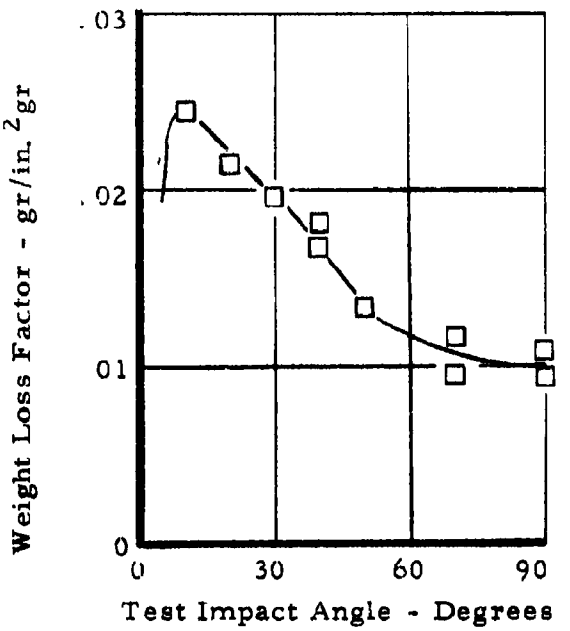

FIGURE 11. WEIGHT LOSS FACTOR VERSUS TEST IMPACT ANGLE, PEARLITIC C-1050 STEEL, AIR VELOCITY 835 FPS, DUST CONCENTRATION 0.013 GR/FT^3, 0 - 74 MICRON SILICA FLOUR

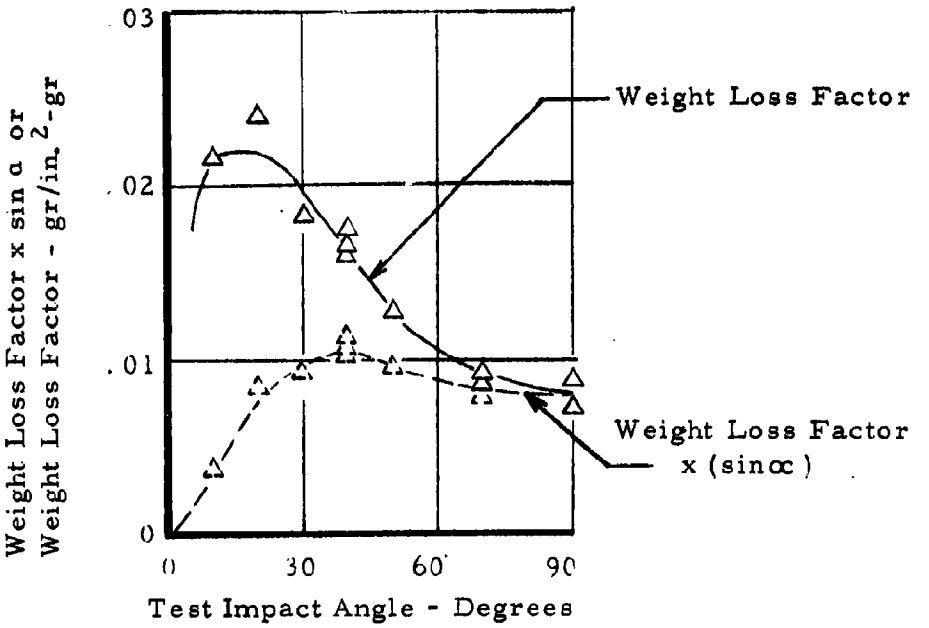

FIGURE 12. WEIGHT LOSS FACTOR VERSUS TEST IMPACT ANGLE, TEMPERED C-1050 STEEL, AIR VELOCITY 835 FPS, DUST CONCENTRATION 0.013 GR/FT^3, 0 - 74 MICRON SILICA FLOUR

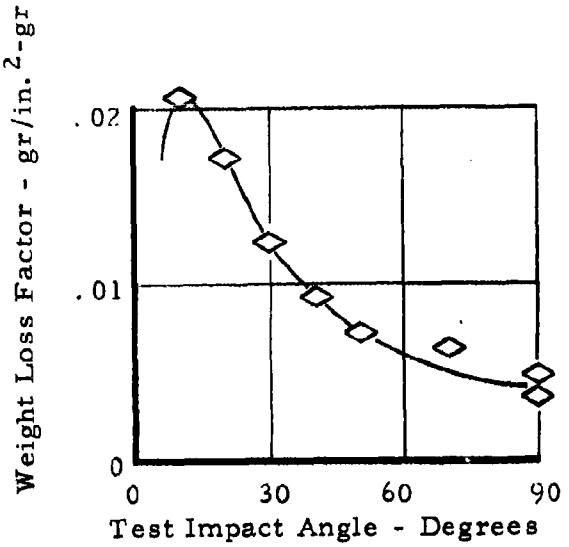

FIGURE 13. WEIGHT LOSS FACTOR VERSUS TEST IMPACT ANGLE, 6061-T6 ALUMINUM ALLOY, AIR VELOCITY 835 FPS, DUST CONCENTRATION 0.013 GR/FT^3, 0 - 74 MICRON SILICA FLOUR

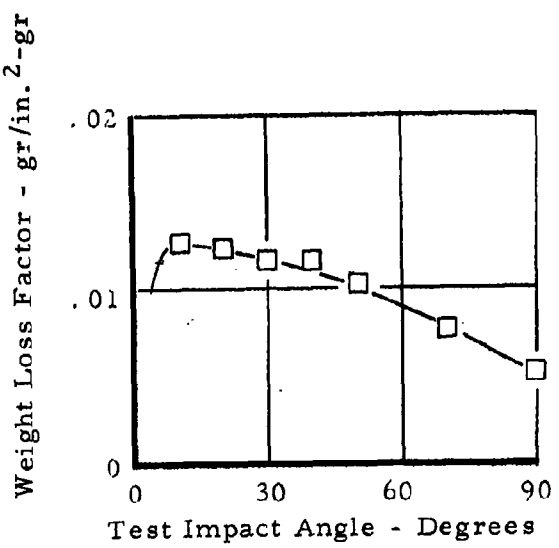

FIGURE 14. WEIGHT LOSS FACTOR VERSUS TEST IMPACT ANGLE, PEARLITIC C-1050 STEEL, AIR VELOCITY 835 FPS, DUST CONCENTRATION 0.013 GR/FT^3, SAE TEST DUST, COARSE GRADE

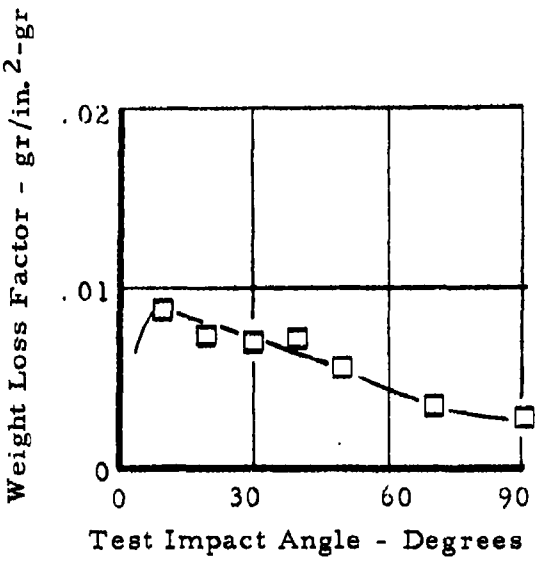

FIGURE 15. WEIGHT LOSS FACTOR VERSUS TEST IMPACT ANGLE, PEARLITIC C-1050 STEEL, AIR VELOCITY 835 FPS, DUST CONCENTRATION 0.013 GR/FT^3, SAE TEST DUST, FINE GRADE

from the expression for the weight loss factor, it is seen that the sin θ appears in the denominator. At low impact angles, a small change in the test angle of impact θ has a large effect upon the reciprocal of the sin θ. Thus, a small error in test angle of impact causes a small error in the location of the datum point along the abscissa, and a relatively large error in its location along the ordinate. Small errors in test angle were difficult to prevent, the small size of the specimen making very accurate installation and alignment difficult. Erosion of the specimen holder also contributed to errors in test angle. To aid in plotting the data, the weight loss factor for each point was multipled by the sin of the corresponding impact angle, and these points were plotted with dashed lines. A best fit curve was easily drawn through these points, since errors in the weight loss factor due to test impact angle errors were greatly decreased. The points on the dashed curve were then divided by sin θ and thus transferred to weight loss factor coordinates as the curve of best fit.

Figures 7 through 15 show the trends predicted by Finnie's derivation. As the angle of impact decreases from 90°, the erosion rate increases to a maximum, then abruptly drops towards zero at an impact angle of zero degrees. Agreement between the theoretical analysis and experiment is generally good, the poorest agreement occurring at high impact angles. This is due to the fact that at high test impact angles, the dust particles strike the specimen at angles lower than the test angle due to the change in the direction of the air stream in the neighborhood of the specimen. In addition, the surface of the specimen is pitted from prior impacts, and the actual impact angle of a given particle will be affected by the shape of these pits. These two factors contribute to the excess of experimental erosion over the predicted trend.

The data shown represent tests conducted using two different air-stream velocities. The data taken at the lower velocity (Figs. 7 - 9) exhibit maximum erosion rates at an erosion angle of approximately 20°. The higher air velocity plots (Figs. 9 - 15), on the other hand, indicate that maximum erosion occurs at an angle in the neighborhood of 10°. From Equation (18) and the subsequent discussion, it is seen that the angle of maximum erosion is a function of the geometry of the eroding particle, and does not depend on the impact velocity. It would be expected, therefore, that the angle for maximum erosion would be equal for the two types of tests. The reason for this inconsistency seems to be, again, a consequence of the actual impact angle being consistently smaller than the test angle. For lower velocities, this effect is more pronounced, and results in the maximum point being shifted towards higher angles. Thus, it seems probable that the correct angle for maximum erosion is more nearly that shown for the higher velocity tests than for the lower.

Figures 14 and 15 show data obtained using SAE test dust, coarse grade and fine grade respectively. All the other curves represent data resulting from erosion by the silica flour. It is seen that the general shape of the curves for SAE test dust is somewhat different from those for silica flour, although the angles for maximum erosion rate are approximately equal. This is construed to mean that the values of P [see Eq. (18)] for each dust type are approximately the same, since the angle of maximum erosion depends only on the value of P. Since the SAE test dust is a natural dust that has been subjected to weathering, and the silica flour is artificially crushed, it would be expected that the silica flour would exhibit a higher degree of angularity than the SAE test dust. Microscopic examination does not reveal a marked difference in angularity between the two; however, undetected differences in angularity may contribute to significant differences in erosion capabilities. In addition, mineral composition and particle size distribution differ in the two dust types, and this doubtlessly contributes to the difference in the shape of the two sets of curves.

C. Erosion Wear Patterns

An interesting phenomenon observed during dust erosion tests on gas turbines previously conducted at Southwest Research Institute[1] was the surface ripples formed on gas turbine components that had experienced high rates of erosion. These ripples were particularly striking on the compressor impeller (2025T6 aluminum alloy) and compressor diffuser (QQ-A-601) Class 3M, Condition T6 Aluminum Alloy . The ripples were observed to form in locations where the impact angle was low and the particle velocity high. The ripples extend in roughly parallel lines perpendicular to the direction of air flow. No ripples were observed with small size ranges of dust, but were common when the dust used was in the size range of 0 - 74 microns.

Similar ripple patterns were observed during the present series of tests. The first observation was made on martensitic C-1050 steel specimens subjected to erosion at a 90° impact angle. The patterns were rough concentric circles with the center of the circles coinciding with the specimen center. The amplitude of the ripples were on the order of 10 microns, the wavelength approximately 4 mm. After conducting erosion tests on a lead specimen at an impact angle of 40°, relatively deep, well-defined patterns were visible. Figure 16 is a photograph of this specimen. The ripples represented in Figure 16 have a wavelength of approximately 0.16 mm.

Consideration of the equations of motion for a single abrasive particle leads to a possible explanation of the formulation of these wear patterns. From the equations of motion for a single abrasive particle (Eqs. 9 and 10).

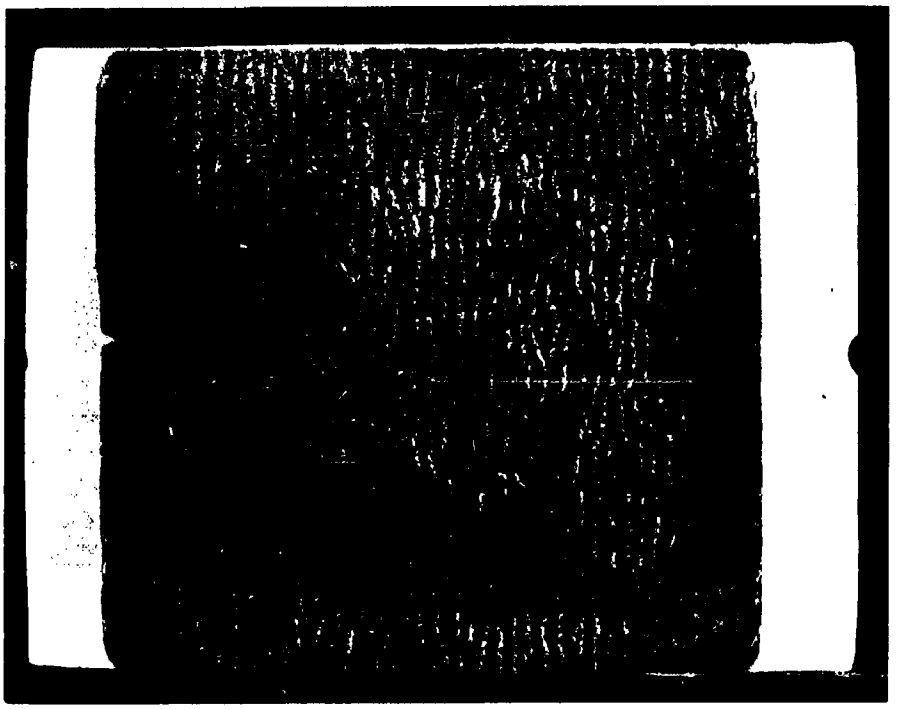

FIGURE 16. EROSION RIPPLE PATTERN-LEAD SPECIMEN

the horizontal and vertical components of the particle velocity may be found at the instant the particle leaves the specimen surface

$$\dot{x}'_T = V \cos \alpha - \frac{2}{P} V \sin \alpha$$

$$\dot{y}_T = -V \sin \alpha$$

These results are valid for $0 < \alpha < \tan^{-1} P/2$. For small values of α, it is seen that the horizontal velocity component may take on significant values. It is thought that the ripple wear patterns are a result of the skipping motion of the individual particles, a motion much like that of a flat stone skipping across a calm surface of water. For the case of the dust particle, however, the particle will gain additional velocity from the air stream as it rises after leaving the specimen surface. The particle is then directed back down onto the specimen surface by the airstream. In experiments with lead specimens oriented at 40° to the airstream the ripples were found to be deepest and most distinct adjacent to and downstream from a discontinuity consisting of a gap between the specimen and the specimen holder. Deep scratches cut into into the lead specimen caused similar deep distinct ripples leading to the theory that the discontinuities are the origin of the ripple patterns. Once the pattern is originated, it is stable, since each ripple becomes a source for further rippling downstream. The rippling pattern is observed to decay and lose its regularity at points far from the originating discontinuity. As erosion continues, the ripples become deeper and more distinct.

At first, the concentric ripples on the martensitic steel specimen did not seem to reinforce this theory due to the absence of an originating discontinuity. However, microscopic examination of several martensitic steel specimens showed that all had a very shallow dimple in the center of the specimen, probably a result of the severe heat treating quench. Thus, particles striking near the center of the specimen were then accelerated along the surface of the specimen by the airstream, encountered the edge of the dimple, and rebounded to begin the wear pattern.

It should be noted that the presence of a deep ripple pattern on the specimen surface would be expected to confuse the effect of test impact angle upon erosion rates. This was not verified since no angle of impact data was obtained for lead, and the depth of the ripple pattern on other specimens was so small as to have negligible effect on erosion rates.

The fact that each dust particle makes multiple impacts on the specimen surface will tend to make the test angle of impact versus erosion

rate curves more flat, and will contribute to the observed erosion at a test angle of 90°, in contradiction to the theoretical analysis.

D. Velocity Effect

From the derivation for material removal by a single abrasive particle, it would be expected that the material removed will vary as the particle velocity squared. The results of several erosion tests with air velocity as the independent variable are shown in Figure 17 through 20. These results show that the predicted relationship is borne out extremely well for a test impact angle of 40°, and less well for a test impact angle of 90°.

At first consideration, it would seem that the differences in air velocity and actual particle velocity would cause the results shown to be in considerable error when considering the effects of actual particle velocity upon erosion rate. However, Figure 3 shows that, to a very good approximation, the particle velocity is a linear function of the airstream velocity. Denoting the various sizes of particles in the airstream by subscripts

$$\begin{aligned} V_1 &= C_1 W \\ V_2 &= C_2 W \\ &\cdots \\ V_z &= C_z W \end{aligned} \qquad (19)$$

where C is a constant of proportionality. Assuming that for each size of particle, the erosion rate varies as the nth power of the velocity, the weight loss factor is given by

$$w = (k_1 V_1^n m_1 + k_2 V_2^n m_2 + \ldots + k_z V_z^n m_z)\frac{1}{M} \qquad (20)$$

where k is a constant. Substituting Equation (19) into Equation (20) and collecting terms gives

$$w = (k_1 C_1^n m_1 + k_2 C_2^n m_2 + \ldots + k_z C_z^n m_z)\frac{W^n}{M} \qquad (21)$$

or w = (constant) (W^n). This shows that the slope of the weight loss-airstream velocity curve will accurately reflect the actual weight loss-particle velocity power relationship. The difference in airstream velocity

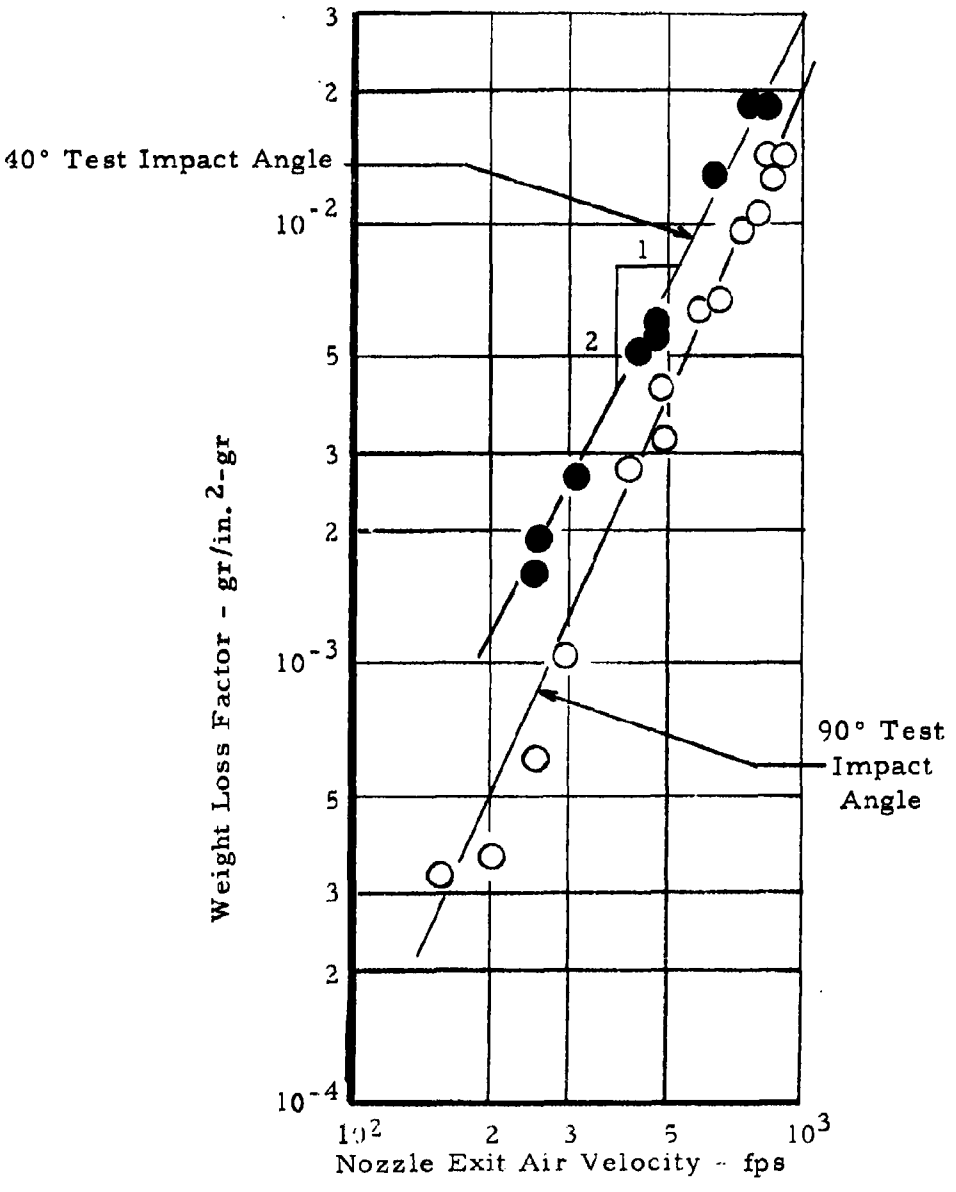

FIGURE 17. WEIGHT LOSS FACTOR VERSUS AIR VELOCITY MARTENSITIC C-1050 STEEL, DUST CONCENTRATION 0.013 GR/FT^3, 0 - 74 MICRON SILICA FLOUR

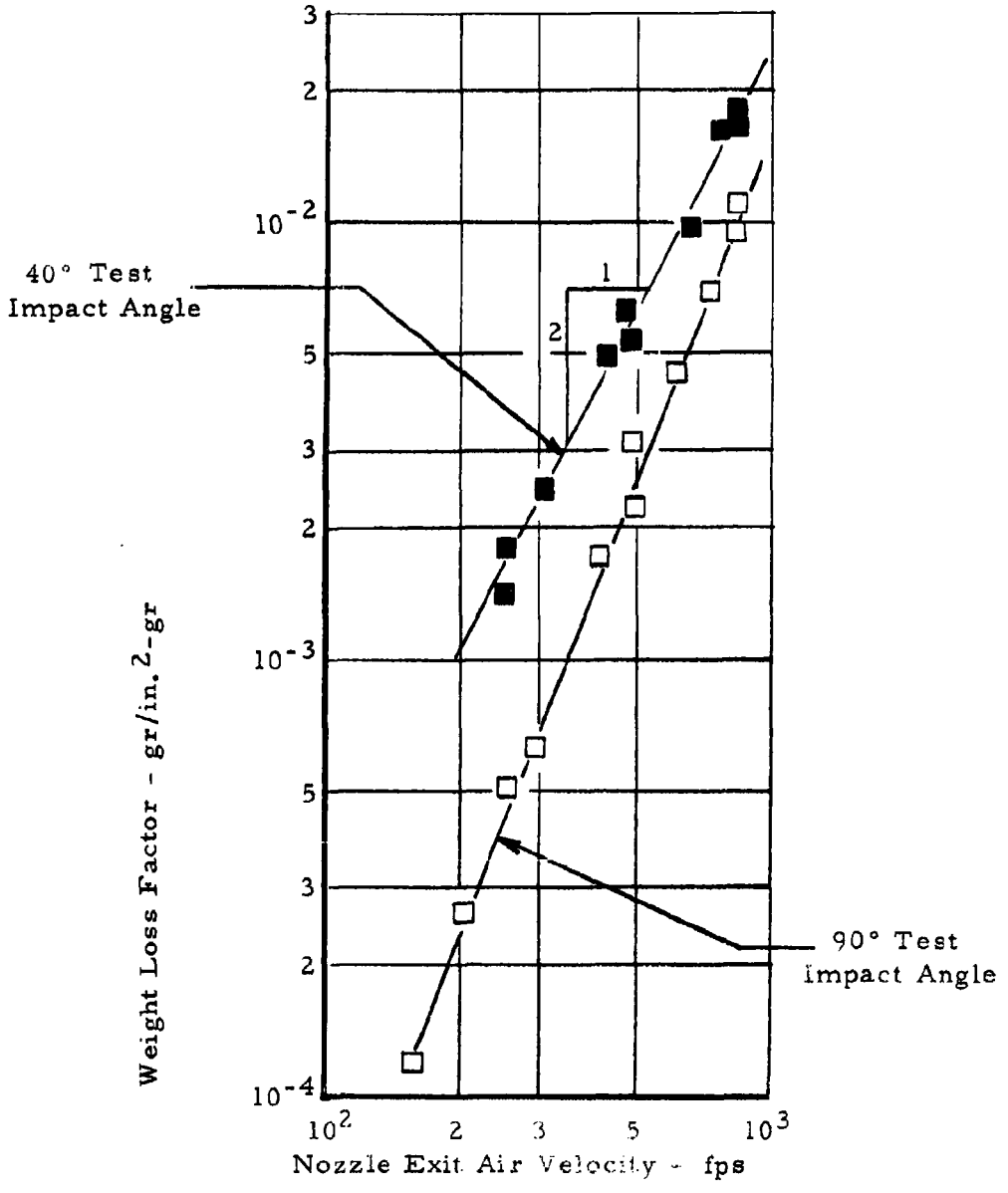

FIGURE 18. WEIGHT LOSS FACTOR VERSUS AIR VELOCITY PEARLITIC C-1050 STEEL, DUST CONCENTRATION 0.013 GR/FT^3, 0 - 74 MICRON SILICA FLOUR

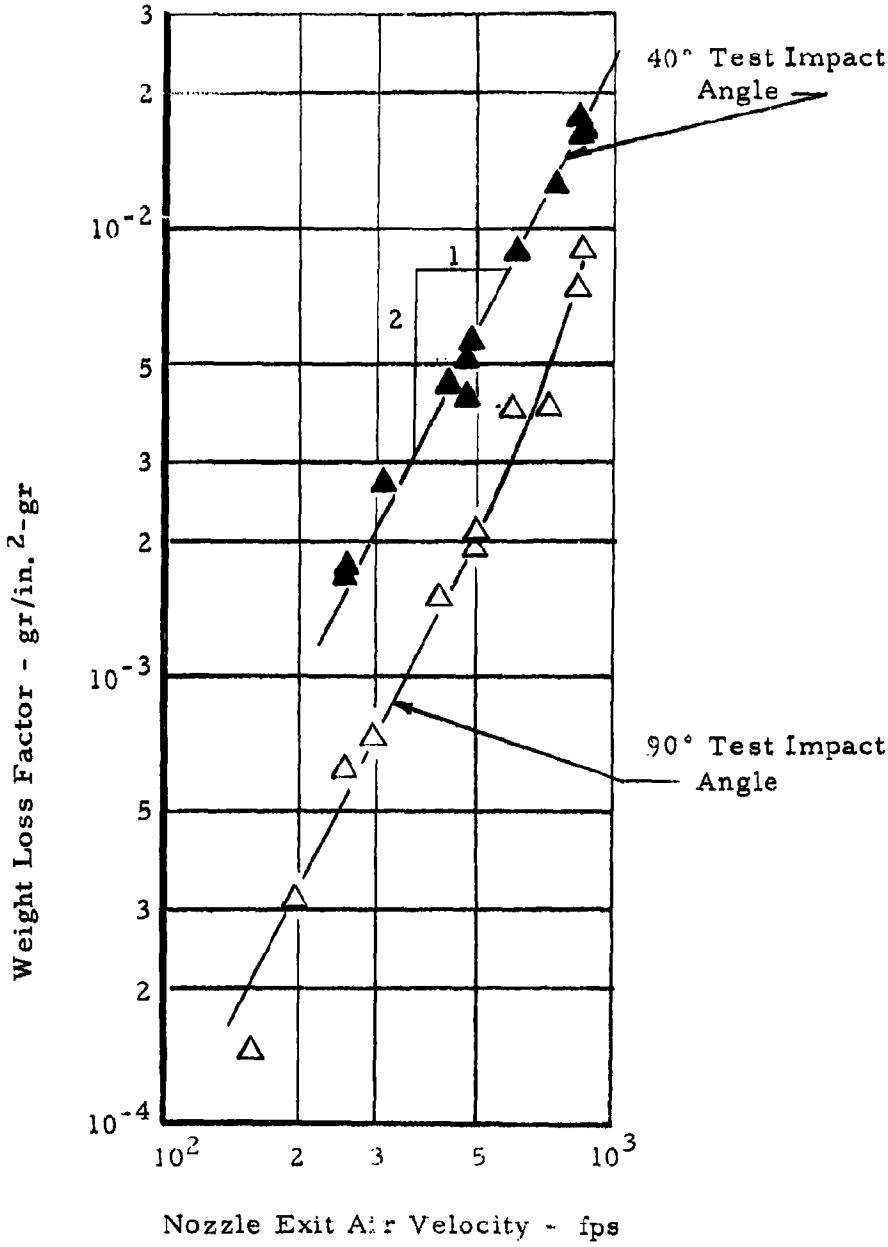

FIGURE 19. WEIGHT LOSS FACTOR VERSUS AIR VELOCITY TEMPERED C-1050 STEEL, DUST CONCENTRATION 0.013 GR/FT^3, 0 - 74 MICRON SILICA FLOUR

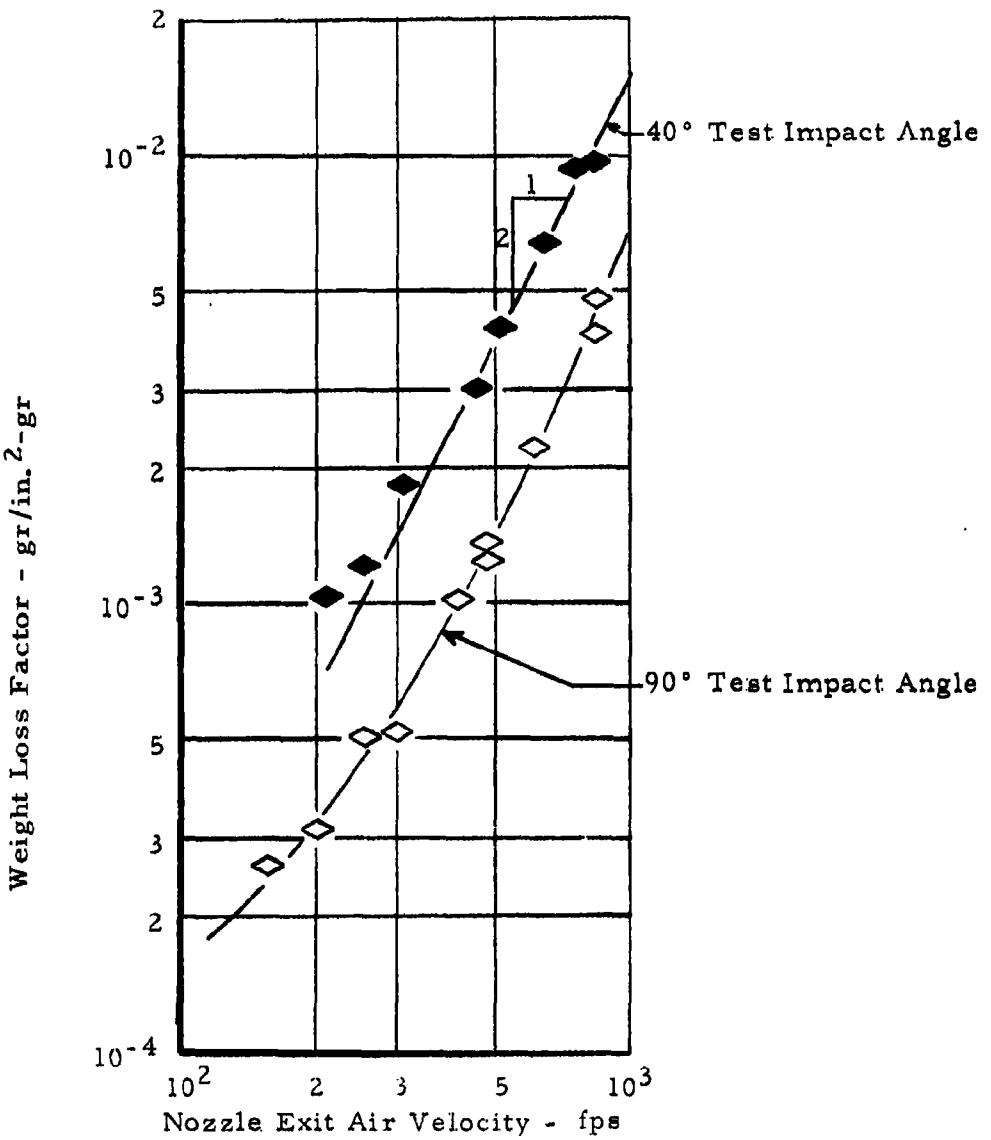

FIGURE 20. WEIGHT LOSS FACTOR VERSUS AIR VELOCITY 6061-T6 ALUMINUM ALLOY, DUST CONCENTRATION 0.013 GR/FT^3, 0 - 74 MICRON SILICA FLOUR

and particle velocity will not, therefore, cause an appreciable error in the slope of the weight loss-air velocity curves.

The difference in slope of the weight loss-air velocity curves for a given material at test angles of 40° and 90° is believed to be primarily due to the difference in test angle and particle impact angle. This error, previously discussed, causes the data for the 90° test angle to actually reflect the results of impacts varying from 90° for the larger particles to some lower angle for the smaller particle. This difference in test angle and actual impact angle changes with air velocity, and since the weight loss varies with impact angle for a given particle, the results shown for a 90° test angle probably do not accurately represent the true velocity effect. This error is greatly reduced for lower test angles, and the data for the 40° test angle provide a more accurate representation of the relationship.

The above results, with the results of the effect of variation in angle of impact, in general show good agreement with the equations derived by Finnie. These equations describe an erosion process characterized by plastic deformation of the material. In another paper[6], Finnie has described the characteristics of erosion of brittle materials. The brittle materials exhibit maximum erosion at impact angles of approximately 90°, the erosion rate then decreasing monotonously to zero at a 0° impact angle. In addition, the erosion rate of brittle materials varies as the particle velocity taken to a power greater than two. For instance, it was found that erosion of porcelain showed $w \sim V^{3.3}$, and in tests of brittle steel, the exponent varied between 5.5 and 6.5. In the present study, the brittle type of erosion was not encountered. It is interesting to note that during erosion tests conducted by Finnie using particles of 60-mesh (250 micron) silicon carbide, it was found that C-1055 SAE steel hardened to Rockwell C 63 showed the characteristics of a brittle material. In the present study, a nearly identical material (martensitic C-1050 SAE steel, Rockwell C 62) shows the erosion characteristics of a ductile material. This indicates that the line of separation between brittle and ductile materials is not a definite one, and may depend a great deal on abrasive particle size and/or shape.

It should be noted that a wide range of materials falling within the class of ductile materials as applied to dust erosion would be fortunate from the viewpoint of an investigator, since the mechanism of erosion of brittle materials appears to be difficult to explain. This mechanism appears to involve displacement of material by the abrasive particle, but in addition the propagation and intersection of cracks makes an important contribution. A detailed analysis of this latter mechanism is not available at the present time.

E. Concentration Effect

Several tests were made to determine the effect of dust concentration upon the erosion rate of various materials. Intuitively, it would be expected that the weight loss factor would be independent of dust concentration; that is, an increase in dust concentration would cause a proportionate increase in erosion weight loss, and the weight loss factor would remain constant.

Figures 21 and 22 show the experimental results. It is seen that there is a definite tendency for the weight loss factor to increase as concentration increases. Although the change in the weight loss factor is relatively small, the phenomenon is of interest, and some possible explanations will be discussed.

The most obvious reason for the concentration effect observed is that the increased concentration causes mutual interference between particles such as collisions or agglomeration of several particles into a large low-velocity mass. If this were actually occurring, however, the percentage reduction in weight loss for a given increase in concentration should be the same for each material. From the curves, it is seen that this does not hold true, when comparing the results for aluminum with those for the steel specimens. The percentage change in the weight loss factor for aluminum is much larger than for the steels.

As the dust concentration is increased and all other variables held constant, the net effect upon the specimen is a higher frequency of impact of the dust particles. The cause for the observed result therefore must be related to the time rate of change of some variable that affects erosion rate.

A possible explanation of the observed results involves the work hardening of the specimen material in the neighborhood of the particle impact. As is discussed in another section of this report, the heat generated by the impacting particle results in rather high temperatures in the specimen material near the cutting tip of the particle. It seems reasonable to assume that any work hardening of the specimen due to the deformation of the surface by the impacting particle will decrease with time, due to the high temperature levels. A second particle impacting in the deformed region immediately after the first impact would encounter a material of higher hardness than a particle that impacted at some later time. Thus, a high dust concentration may maintain a higher specimen surface hardness than a low dust concentration with a resulting lower rate of erosion.

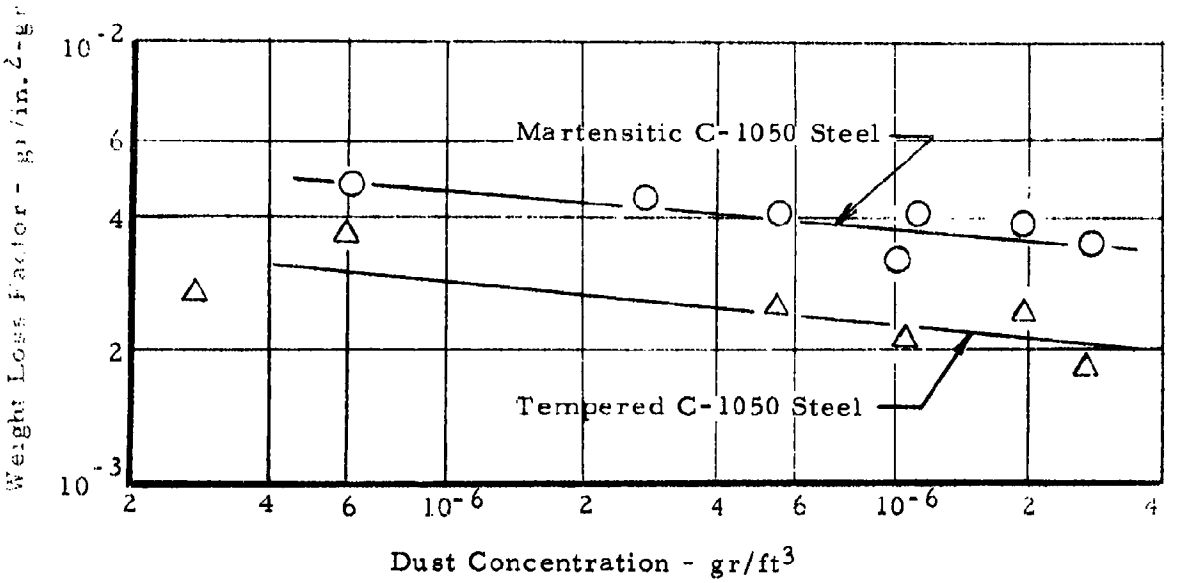

FIGURE 21. WEIGHT LOSS FACTOR VERSUS DUST CONCENTRATION, AIR VELOCITY 475 FPS, TEST IMPACT ANGLE 90°, 0 - 74 MICRON SILICA FLOUR

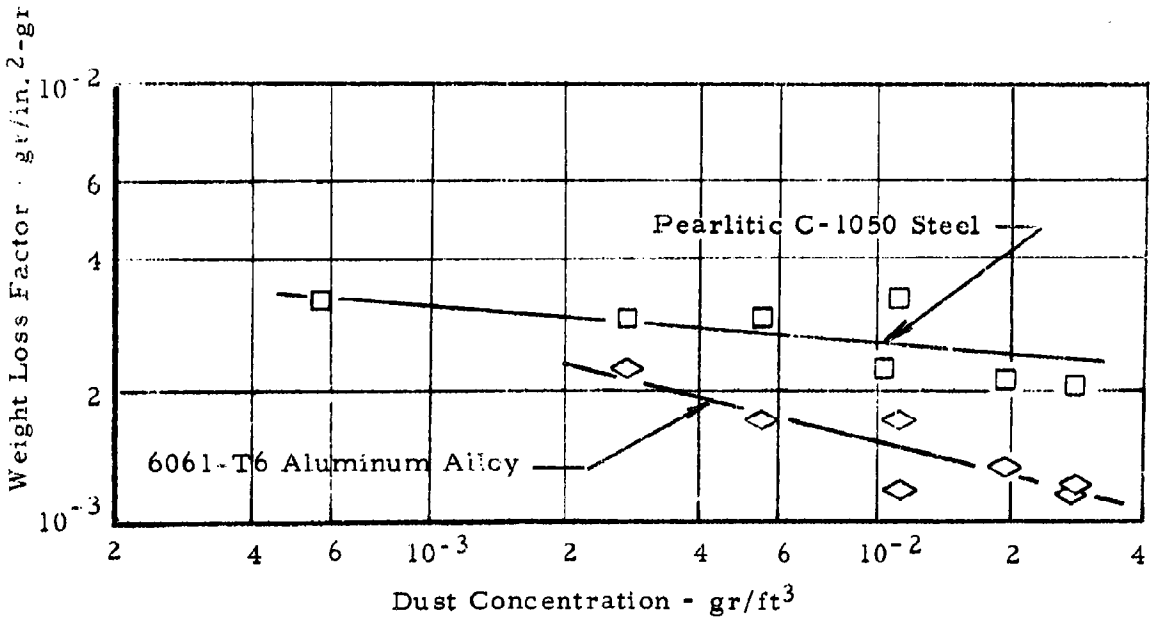

FIGURE 22. WEIGHT LOSS FACTOR VERSUS DUST CONCENTRATION, AIR VELOCITY 475 FPS, TEST IMPACT ANGLE 90°, 0 - 74 MICRON SILICA FLOUR

A second explanation involves consideration of the formation of oxides on the specimen surface. Outwater and Shaw[7], while performing grinding tests in an inert atmosphere, observed an increase of grinding forces up to 25 times that experienced in an atmosphere of air. This result was attributed to the absence of an oxide film on the freshly cut surfaces in the inert atmosphere, resulting in the rewelding of small chips to the specimen surface as they curled back onto the surface during further cutting. This suggests an explanation for the concentration effect noted during erosion tests. From the size distribution of the 0 - 74 micron dust, it can be calculated that there are approximately 4.5×10^9 dust particles over 1.8 microns in diameter per gram of dust. For the test conditions of Figures 21 and 22, it may be estimated that roughly from 1 to 100 particles over 1.8 microns in diameter strike within an area of 100 square microns each second, the range of impact frequency being due to the variation in the test concentration. It seems reasonable to assume that as the impact frequency (concentration) increases, more and more often there will be occasions in which insufficient time exists between impacts for an oxide film to form, resulting in minute particles of material rewelding to the surface with the corresponding decrease in weight loss.

The experimental data does not permit a choice between these theories. It is interesting to note, however, that the aluminum alloy, which is well known for its ability to rapidly form an oxide film, exhibits a greater change in weight loss factor per unit change in concentration than does steel. This could be interpreted to mean that for a decrease in impact frequency, the aluminum is able to form a protective film more rapidly than steel, resulting in a greater relative decrease in the aluminum erosion loss.

There is a possibility that further study of the observed concentration effect would increase understanding of the mechanism involved, and the subsequent control of the mechanism, perhaps by proper choice of materials or material coatings, could result in a substantial decrease in erosion rates.

F. Dust Size Effect

Several series of tests were conducted to define the relative effect of the different dust size ranges upon the rate of erosion. A typical set of results is shown in Figure 23. This chart shows the variation in weight loss factor for a constant airstream velocity. From previous discussions, it will be evident that these results will not accurately reflect the erosion capabilities of the dust at a constant particle velocity since the larger

particles do not attain airstream velocity. However, with information previously obtained, it is possible to correct the test results to show the size effect at a constant particle velocity. This is done by using Equation (21), rewritten below

$$w = (k_1 C_1^n m_1 + k_2 C_2^n m_2 + \ldots + k_z C_z^n m_z) \frac{W^n}{M} \qquad (21)$$

Equation (21) represents the contributions of increments of size ranges of dust to the weight loss factor. Five size increments were used, the first being the size range represented by the 0 - 5 micron dust, and the remaining four were the size range increments represented by the difference between the maximum particle diameters of the 0 - 5 and 0 - 10 micron dust, the 0 - 10 and 0 - 43 micron dust, and so on. For each size range of dust, Equation (21) was written. The constant C was obtained from Figure 3 or from Equation (5). The weight of dust m in the size increments was obtained from Figure 2. Thus, for the 0 - 5 dust, Equation (21) is written containing only one term

$$w = \frac{m_1 k_1 C_1^2 W^2}{M}$$

For the 0 - 10 micron dust, Equation (21) contains two terms, and so on. The weight loss factor w for each case is taken from the experimental data. The five equations have five unknowns, the k factors. These are obtained by solution of the equations; the equations are rewritten letting the constants C_1, C_2, C_3 be unity, and the corrected weight loss factor is obtained. This corrected weight loss factor represents the erosion for a constant particle velocity. The corrections are shown in Figures 23 and 24 as dashed lines. The corrections for the 0 - 5 and 0 - 10 micron dust were negligible.

Figure 23 shows that the weight loss factor first increases rapidly as the dust size range increases, and then becomes fairly constant for size ranges greater than 0 - 43 microns. At first, this seems to indicate that the 0 - 150 micron dust is not significantly more damaging than 0 - 43 micron dust. This statement is true, as long as the erosion rate is specified in terms of unit weight of dust. That is, all other variables held constant, a gram of 0 - 150 dust will cause approximately the same erosion as a gram of 0 - 43 micron dust. More significant, however, is a plot of the erosion rate on a per impact basis. Using the data shown on the dust size distribution curve, Figure 2, and assuming particle sphericity, the number of dust particles per gram of dust for each size range of dust may be

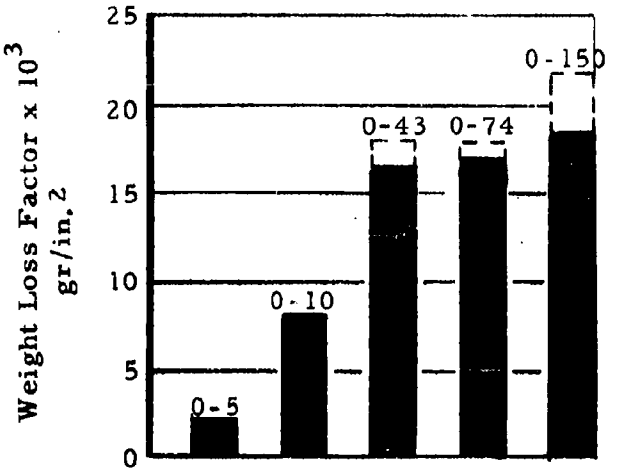

FIGURE 23. WEIGHT LOSS FACTOR VERSUS DUST PARTICLE SIZE RANGE, AIR VELOCITY 850 FPS, DUST CONCENTRATION 0.013 GR/FT^3, PEARLITIC C-1050 STEEL, 40° TEST IMPACT ANGLE, SILICA FLOUR

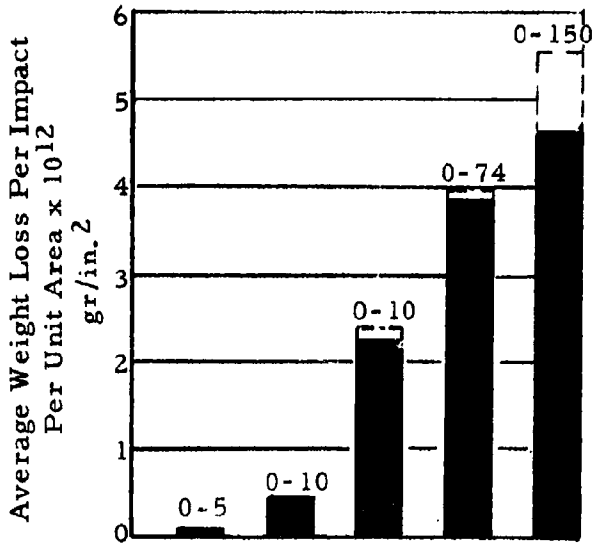

FIGURE 24. AVERAGE WEIGHT LOSS PER IMPACT VERSUS DUST PARTICLE SIZE RANGE, AIR VELOCITY 850 FPS, DUST CONCENTRATION 0.013 GR/FT^3, PEARLITIC C-1050 STEEL 40 ° TEST IMPACT ANGLE, SILICA FLOUR

calculated. Dividing the weight loss factor by the number of particles per gram of dust gives an average weight loss per particle. Figure 24 shows a plot using this erosion parameter. The results now show continuously increasing erosion with increasing size range, a result intuitively expected.

The theoretical equations for volume removal by a single particle [Eqs. (16) and (17)] indicate that for a particle with a moment of inertia proportional to mr^2, the volume removed is proportional to the particle mass, or to the diameter cubed. It is expected that tests using particles of one diameter (instead of a range of diameters) will show this trend, providing the particles are relatively similar in geometry. It is emphasized that the data shown here are for the specific size ranges of dust shown in Figure 2, and should not be used to predict erosion losses for a particular dust particle diameter, or for dust distributions significantly different from those used in this study.

C. Material Properties Effect

In Finnie's equations for volume removal by a single abrasive particle [Eqs. (16) and (17)], it is seen that the effect of material properties is included by means of the plastic flow stress term, p. The plastic flow stress of a material is often equated to the material hardness measured by the Brinell method or an equivalent. Thus, it would be expected that the volume removed in an erosion test would be inversely proportional to the hardness of the materials tested, other variables held constant. Figure 25 is a plot of volume loss factor versus Knoop hardness for several materials. The general shape of this curve was verified by several tests at different air velocities and test impact angles. The data shown are typical of all these tests. The plot indicates that the inverse relationship could conceivably be valid for very low material hardnesses, but is definitely not of use throughout most of the range of hardnesses of common engineering materials. (It should be noted that this difficulty does not affect the validity of Finnie's equations, and only shows that the plastic flow stress used in the equations is not equivalent to material hardness for the materials tested.) Figure 25 indicates fair correlation between erosion rate and material hardness, but fails to explain the high erosion rate for the martensitic steel, and the low rate for the tempered steel.

In attempting to better correlate erosion rates with material properties, several dimensional analyses were conducted. Both mechanical and thermal properties of the materials were used as variables. Variables used in the analyses were material hardness, material density, particle impact velocity, material thermal conductivity, material specific heat,

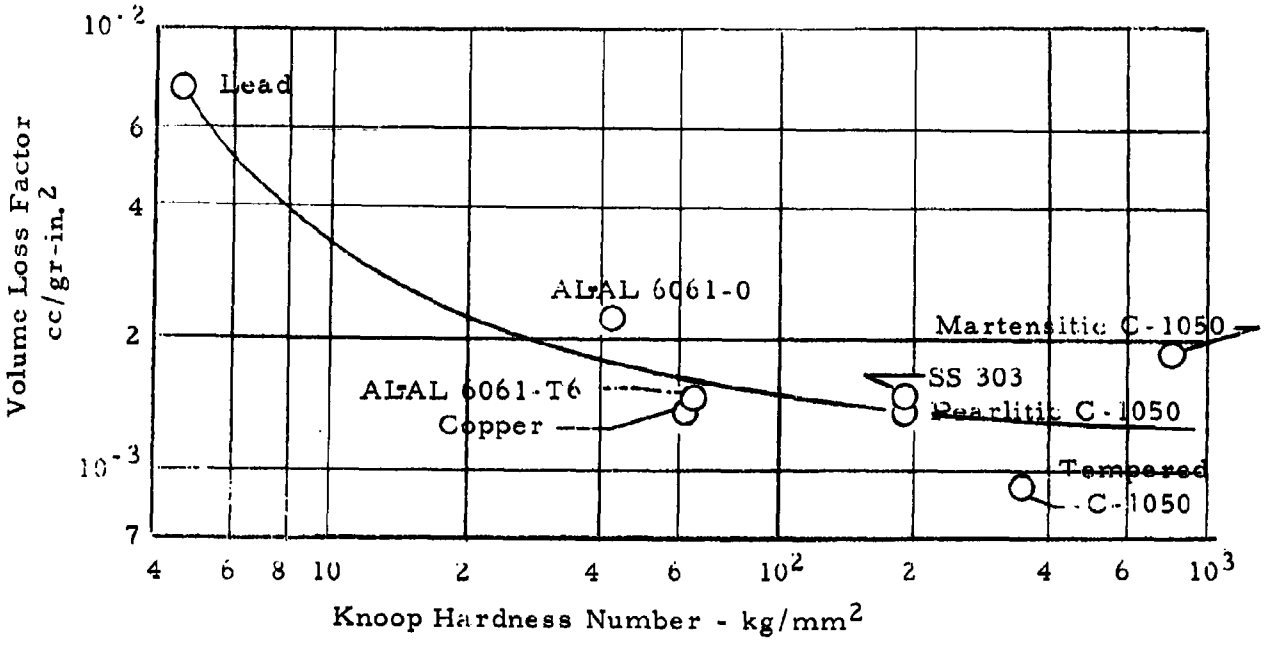

FIGURE 25. VOLUME LOSS FACTOR VERSUS KNOOP HARDNESS NUMBER, AIRSTREAM VELOCITY 835 FPS, 0 - 74 MICRON SILICA FLOUR, DUST CONCENTRATION 0.013 GR/FT^3, 90° IMPACT ANGLE

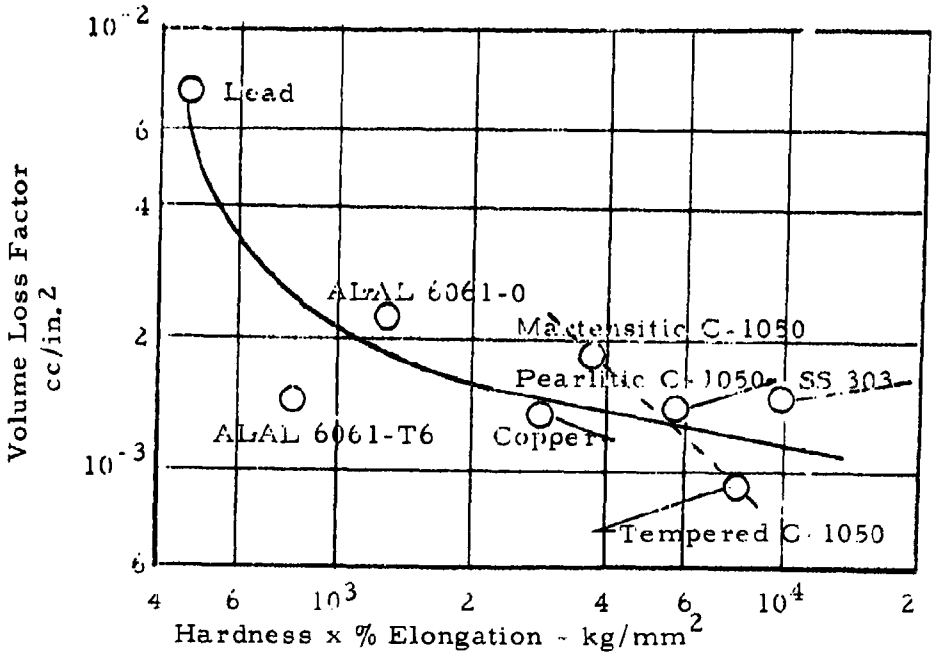

FIGURE 26. VOLUME LOSS FACTOR VERSUS KNOOP HARDNESS NUMBER X % ELONGATION, AIRSTREAM VELOCITY 835 FPS, 0 - 74 MICRON SILICA FLOUR, DUST CONCENTRATION 0.013 GR/FT^3, 90° IMPACT ANGLE

reduction of area of material as found in standard tensile test, modulus of elasticity, and others. Various dimensional groups were obtained, but no satisfactory correlation was found.

From the relative erosion rates of the various steel specimens, it appeared that the strain energy required to fracture was an important variable. Since material hardness is a measure of tensile strength, the product of hardness and percent elongation represents an approximation of the area under the stress-strain curve, or the strain energy to fracture. Figure 26 shows a plot using this variable. The C-1050 steel specimens now have a reasonable relation, but the overall correlation is not greatly improved. Some reasons for the difficulties discussed here will now be considered.

In the past, considerable work has been done on the mechanisms of material removal in the grinding process[7,8], with some very interesting results. Comparison of the grinding process with the erosion of materials by small particles shows considerable similarity between the two. The depth of cut of the abrasive grains in the material is of the same order of magnitude and the speed of cutting is also similar. For the grinding process, Backer, Marshall, and Shaw[8] have demonstrated that the specific energy of material removal (the energy required to remove a unit volume of material) is extremely high, and corresponds to a material strength equal to the theoretical material strength. This theoretical strength may be calculated by considering the attractive and repulsive forces of atoms in adjacent rows of a perfect crystal lattice. The theoretical strength of a given material can be shown to be approximately equal to $G/2\pi$, where G is the shear modulus of the material. The theoretical strength is therefore not affected by changes in hardness or other properties that do not involve a change in G. For steel, the theoretical strength is about 1.8×10^6 psi, compared to values of about 50,000 psi found in tensile tests for mild steel. It is thought that the difference in these two values may be due to the imperfections (grain boundaries, crystal defects, and impurities) actually present in the material. However, in the grinding process, the depth of cut is of the same order of magnitude as the mean distance between imperfections, and the material is able to demonstrate its theoretical strength. This effect is shown in Figure 27 for the grinding process. These results indicate that for depths of cut less than about 28 microinches, the specific energy remains constant at its theoretical value.

For several dust erosion tests, the depth of erosion pits on the specimen surfaces were measured with a Talysurf surface measuring instrument. The average pit depths for steel specimens ranged from about 20 microinches for the lower air velocities to 50 microinches for air

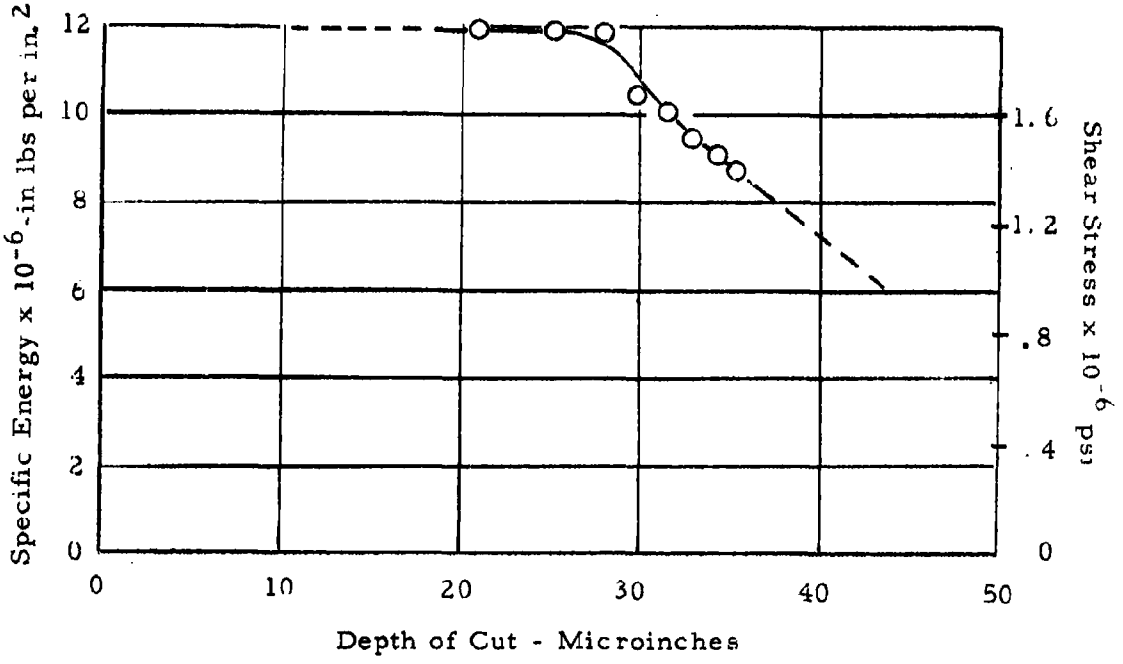

FIGURE 27. SPECIFIC ENERGY OF VOLUME REMOVAL VERSUS DEPTH OF CUT FOR GRINDING TESTS - BACKER, MARSHALL AND SHAW, REFERENCE 8

velocities of 850 fps. It seems likely that a significant percentage of the total number of impacts result in pit depths much small than this, since the smaller pits are obscured by the larger in the surface analysis. It would therefore be expected that the specific energies involved would be high, approaching the theoretical limit. This is indicated in the present study. The specific energy for several tests was calculated by computing the particle kinetic energy used in removing unit volume of material. For steel, the values obtained ranged from about 3×10^7 in.-lb per cu in. to 9×10^7 in.-lb per cu in. The fact that these values are higher than those obtained in grinding tests is reasonable when it is considered that many of the particles are ineffective in removing material due to unfavorable impact angles, and that many of the particles rebound from the specimen retaining a portion of their original kinetic energy.

The effect of these considerations upon the erosion mechanism may be visualized as follows: The smaller dust particles, when able to remove material from the specimen, are forced to do so at stresses near the theoretical strength of the material. The larger particles are able to cut the material at lower stresses, dependent on the depth of cut and the properties of the material. To obtain a better correlation between material properties and erosion rate, it would seem that the most straightforward approach would be a series of tests using particles of essentially the same size for each test, rather than a wide range of sizes as was done in this investigation. This would enable the investigator to separate the erosion occurring at the theoretical limit due to small particles from that occurring at lesser stresses due to the larger particles. A more favorable condition for determining the material properties controlling the latter type of erosion would then exist.

The results of material property studies as applied to dust erosion will be influenced by the temperatures generated by the cutting particle. Outwater and Shaw[7] have shown that for grinding steel, temperatures over 2000°F are probable in the neighborhood of the cutting edge of the particle. During dust erosion tests on a martensitic C-1050 steel specimen, sparks were observed downstream from the specimen. These sparks seemed to originate about six inches from the specimen and caused a brief streak of light. The presence of these sparks indicates a high material temperature due to the friction forces of cutting. It would be expected therefore, that the high temperature properties of the material will be significant in determining the characteristics of materials with respect to erosion by dust.

Outwater and Shaw[7] indicate that the mean temperature attained during the grinding process is a function of the shear energy of the cutting

process, the specific heat of the material, the geometry of the abrasive particle-specimen system, and the depth of cut. Applied to the erosion process, it may be expected the temperature will not only vary from material to material, but also will vary for a given material from impact to impact due to different depths of cut of the various sizes of particles.

To summarize the results discussed in this section of the report:

(1) For the materials tested, material hardness does not adequately define the plastic flow stress used in Finnie's equation.

(2) For erosion of materials by air-borne dust, the material theoretical strength is believed to have a considerable effect on the erosion rate.

(3) A fair degree of correlation exists between erosion rate and material fracture energy.

(4) Better correlation of material properties versus erosion rates will probably require knowledge of the high temperature properties of the material.

IV. CONCLUSIONS AND RECOMMENDATIONS

From the results of the study presented in this report, it is concluded that:

(1) The erosion by air-borne dust of the materials considered is a process of plastic displacement of material by the impacting dust particle, and the effects of dust particle velocity and angle of impact upon erosion rates may be adequately described by equations defining the trajectory of the particle through the material.

(2) Contrary to previous acceptance, the concentration of dust in the airstream has a significant effect upon the weight loss factor.

(3) Erosion rates are a strong function of dust particle size, the correlation being best described by consideration of the average erosion loss per particle impact.

(4) The erosion rate of materials is probably affected by the theoretical material strength for the smaller range of particle sizes. A detailed examination of the pertinent material properties applied to dust erosion should consider this, and also the high temperature properties of the material.

It is recommended that further work be done to increase understanding of the relationship between erosion rate, particle size, and material properties. It is believed that this can be carried out most efficiently by experimental work patterned after the present study, but with the addition of equipment to separate dust into small ranges of size. This control over dust size would eliminate many of the difficulties encountered in the present investigation, and would allow the investigator to control more closely impact velocity, impact angle, and particle depth of cut. Such an investigation, it is believed, would provide significant information on the effect of material properties upon erosion rate.

For application to the dust erosion of gas turbines, it is considered essential that further experimentation be done at elevated specimen temperatures, and the effect of specimen temperature upon erosion rate be defined. In addition, the relative abrasiveness of different types of natural dust needs

to be determined for purposes of practical design. From the results of this investigation, it is seen that to completely define the properties of a dust as pertains to erosion, three relations must be given. First, the erosion rate as a function of particle angle of impact for the dust will provide information as to the magnitude of the angle for maximum erosion rate. Second, the relationship between erosion rate and particle size must be defined. This will require separation of the dust sample into narrow size ranges. Third, from the results of the first two tests, the magnitude of the weight loss factor, or a similar parameter, must be determined relative to a standard dust eroding a standard specimen. It is possible that many natural dusts will have common values for one or more of these relationships; however, this should be verified experimentally.

LIST OF REFERENCES

1. Pearson, R. O. and Meriwether, R. F., Effects of Dust Ingestion on Gas Turbine Performance and Endurance, Southwest Research Institute Report No. EE-455, Contract No. DA-44-009-ENG-4542, March 1962.

2. Hafer, C. A., and Skinner, D. J., Definition of the Dust Environment for Purposes of Gas Turbine Ingestion Studies, Phase I, Southwest Research Institute Report No. EE-387, Contract No. DA-44-009-ENG-4542, October 1960.

3. Society of Automotive Engineers, "Air Cleaner Test Code," 1961 SAE Handbook, New York, 1961, p. 820.

4. Dallavalle, J. M., Micromeritics, Pitman Publishing Corp., New York & London, 1948.

5. Finnie, Iain, "The Mechanism of Erosion of Ductile Metals," Proceedings, 3rd U. S. National Congress of Applied Mechanics, pp. 527-532 (1958).

6. Finnie, Iain, "Erosion by Solid Particles in a Fluid Stream," ASTM Special Technical Publication No. 307, 1962, p. 70.

7. Outwater, J. O. and Shaw, M. C., "Surface Temperatures in Grinding," Transactions of the ASME, Vol. 74, No. 1, 1952, pp. 73-86.

8. Backer, W. R., Marshall, E. R. and Shaw, M. C., "The Size Effect in Metal Cutting," Transactions of the ASME, Vol. 74, No. 1, 1952, pp. 61-71.

APPENDIX A

DERIVATION OF PARTICLE DISTANCE-VELOCITY RELATIONSHIP

For a particle being accelerated downward by a fluid stream:

$$F + mg\left(\frac{\rho - \rho_o}{\rho}\right) = m\frac{dV}{dt} \tag{A1}$$

where the drag force F is

$$F = \frac{1}{2}\rho_o (W - V)^2 \bar{A} C_R \tag{A2}$$

The particle Reynold's number is given by

$$R = \frac{\rho_o d}{\mu}(W - V) \tag{A3}$$

The initial particle Reynold's number is

$$R_o = \frac{\rho_o d}{\mu} W \tag{A4}$$

Define the term β as

$$\beta = \frac{2mg\rho_o d}{\mu^2 \bar{A}}\left(\frac{\rho - \rho_o}{\rho}\right) \tag{A5}$$

and let the drag coefficient be

$$C_R = 0.4 + \frac{40}{R} \tag{A6}$$

Combining Equations (A1) through (A6) results in

$$dt = \frac{2md}{\mu\bar{A}} \frac{-dR}{C_R R^2 + \beta} \tag{A7}$$

Integrating (A7) from R_o to R letting

$$S = \sqrt{40^2 - 1.6\beta} \tag{A8}$$

results in

$$t = -\frac{2md}{\mu\bar{A}}\left[\log\left(\frac{.8R + 40 - S}{.8R + 40 + S}\,\frac{.8R_o + 40 + S}{.8R_o + 40 - S}\right)\right] \tag{A9}$$

For the range of air properties and particle sizes used in this report, Equation (A8) reduces to

$$S \approx 40 \tag{A10}$$

Assuming that the particles are spheres

$$m = \frac{\pi d^3}{6}\rho \text{ and } \bar{A} = \frac{\pi d^2}{4} \tag{A11}$$

Equation (A9) may be rearranged to give V explicitly, and integrated to give the distance x traveled by the particle as a function of time t. Substituting Equations (A9), (A10), and (A11) into the equation for x, and rearranging

$$\frac{\rho_o}{\rho}\,\frac{x}{d} = \frac{R_o}{30}\left[\log\frac{R + 100}{R_o + 100}\,\frac{R_o}{R}\right] + 3\,\frac{1}{3}\log\frac{R + 100}{R_o + 100} \tag{A12}$$

APPENDIX B

ESTIMATION OF TRUE IMPACT ANGLE

A sketch of the specimen in the airstream is shown below.

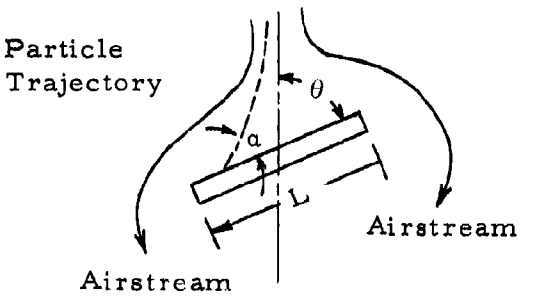

The airstream is shown schematically, and a typical particle trajectory is represented. The number of particles impacting the specimen at any location L per unit specimen area per unit time is

$$N = CV \sin \alpha \tag{B1}$$

where C and V are the local particle concentration and velocity respectively. C and V depend on the conditions of air flow at the specimen, but for a small specimen with a corresponding small airstream disturbance, C and V may be approximated by a constant. Then

$$\sin \alpha = kN \tag{B2}$$

where k is a constant. From consideration of the air flow and the resulting particle trajectories, it is evident that at some location on the specimen, there will exist a stagnation point where the impact angle α is equal to the specimen angle θ. Let this location be designated by L_o. At L_o, then, N will be a maximum, since there is no dilution of the particle concentration by the bending of the airstream. This may be written

$$\text{when } L = L_o,\ \alpha = \theta,\ N = N_{max} \tag{B3}$$

Substituting (B3) into (B2) results in

$$k = \frac{\sin \theta}{N_{max}} \tag{B4}$$

Substituting for k in (B2) gives

$$\sin \alpha = \frac{N}{N_{max}} \sin \theta \tag{B5}$$

Southwest Research Institute, Department of Automotive Research, San Antonio, Texas

A STUDY OF THE BASIC MECHANISM OF DUST EROSION
Charles D. Wood

June 1963. 48 pp with appendixes. Task Order No. 17 (Contract No. DA-23-072-ORD-1375).

This report presents the results of a study of the erosion of materials by air-borne dust. Erosion rates for several metals were obtained over a wide range of dust particle velocity, particle angle of impact, dust particle size, and dust concentration.

The experimental results show that for the range of variables studied, erosion occurs due to the plastic displacement of material by the dust particle. Relationships defining the effect of particle velocity and angle of impact upon erosion rates are given. Experimental data showing the effects of dust concentration, dust size distribution, and material properties on the rates of erosion are presented, and the mechanisms discussed.

UNCLASSIFIED

1. Dust - Erosion by Air-borne
2. Erosion - Mechanisms of Dust

I. DA Project No. 1A025001A622 Task Order No. 17
II. Contract No. DA-23-072-ORD-1375
III. Southwest Research Institute, San Antonio, Texas
IV. Wood, Charles D.
V. Aval fr OTS
VI. In DDC collection

UNCLASSIFIED

Southwest Research Institute, Department of Automotive Research, San Antonio, Texas

A STUDY OF THE BASIC MECHANISM OF DUST EROSION
Charles D. Wood

June 1963. 48 pp with appendixes. Task Order No. 17 (Contract No. DA-23-072-ORD-1375).

This report presents the results of a study of the erosion of materials by air-borne dust. Erosion rates for several metals were obtained over a wide range of dust particle velocity, particle angle of impact, dust particle size, and dust concentration.

The experimental results show that for the range of variables studied, erosion occurs due to the plastic displacement of material by the dust particle. Relationships defining the effect of particle velocity and angle of impact upon erosion rates are given. Experimental data showing the effects of dust concentration, dust size distribution, and material properties on the rates of erosion are presented, and the mechanisms discussed.

UNCLASSIFIED

1. Dust - Erosion by Air-borne
2. Erosion - Mechanisms of Dust

I. DA Project No. 1A025001A622 Task Order No. 17
II. Contract No. DA-23-072-ORD-1375
III. Southwest Research Institute, San Antonio, Texas
IV. Wood, Charles D.
V. Aval fr OTS
VI. In DDC collection

UNCLASSIFIED

Southwest Research Institute, Department of Automotive Research, San Antonio, Texas

A STUDY OF THE BASIC MECHANISM OF DUST EROSION
Charles D. Wood

June 1963. 48 pp with appendixes. Task Order No. 17 (Contract No. DA-23-072-ORD-1375).

This report presents the results of a study of the erosion of materials by air-borne dust. Erosion rates for several metals were obtained over a wide range of dust particle velocity, particle angle of impact, dust particle size, and dust concentration.

The experimental results show that for the range of variables studied, erosion occurs due to the plastic displacement of material by the dust particle. Relationships defining the effect of particle velocity and angle of impact upon erosion rates are given. Experimental data showing the effects of dust concentration, dust size distribution, and material properties on the rates of erosion are presented, and the mechanisms discussed.

UNCLASSIFIED

1. Dust - Erosion by Air-borne
2. Erosion - Mechanisms of Dust

I. DA Project No. 1A025001A622 Task Order No. 17
II. Contract No. DA-23-072-ORD-1375
III. Southwest Research Institute, San Antonio, Texas
IV. Wood, Charles D.
V. Aval fr OTS
VI. In DDC collection

UNCLASSIFIED

Southwest Research Institute, Department of Automotive Research, San Antonio, Texas

A STUDY OF THE BASIC MECHANISM OF DUST EROSION
Charles D. Wood

June 1963. 48 pp with appendixes. Task Order No. 17 (Contract No. DA-23-072-ORD-1375).

This report presents the results of a study of the erosion of materials by air-borne dust. Erosion rates for several metals were obtained over a wide range of dust particle velocity, particle angle of impact, dust particle size, and dust concentration.

The experimental results show that for the range of variables studied, erosion occurs due to the plastic displacement of material by the dust particle. Relationships defining the effect of particle velocity and angle of impact upon erosion rates are given. Experimental data showing the effects of dust concentration, dust size distribution, and material properties on the rates of erosion are presented, and the mechanisms discussed.

UNCLASSIFIED

1. Dust - Erosion by Air-borne
2. Erosion - Mechanisms of Dust

I. DA Project No. 1A025001A622 Task Order No. 17
II. Contract No. DA-23-072-ORD-1375
III. Southwest Research Institute, San Antonio, Texas
IV. Wood, Charles D.
V. Aval fr OTS
VI. In DDC collection

UNCLASSIFIED